

# Monitoring volcano slope instability with Synthetic Aperture Radar: A review and new data from Pacaya (Guatemala) and Stromboli (Italy) volcanoes



Lauren N. Schaefer<sup>a</sup>, Federico Di Traglia<sup>b,\*</sup>, Estelle Chaussard<sup>c</sup>, Zhong Lu<sup>d</sup>, Teresa Nolesini<sup>e</sup>, Nicola Casagli<sup>b</sup>

<sup>a</sup> Department of Geological Sciences, University of Canterbury, Christchurch, New Zealand

<sup>b</sup> Dipartimento di Scienze della Terra, Università degli Studi di Firenze, Florence, Italy

<sup>c</sup> Department of Earth Science, University of Oregon, Eugene, OR, USA

<sup>d</sup> Huffington Department of Earth Sciences, Southern Methodist University, Dallas, United States

<sup>e</sup> Centro per la Protezione Civile, Università degli Studi di Firenze, Florence, Italy

## ARTICLE INFO

### Keywords:

Interferometry  
Ground-based InSAR  
Debris avalanche  
Deformation  
Collapse triggers  
Spreading  
Pacaya  
Stromboli

## ABSTRACT

Volcano slope instability manifests in many forms, ranging from steady state to punctuated movement, or shallow erosion to deep-seated spreading. The interplay of gravity, magmatic or hydrothermal fluids, and often active tectonics on a volcanic edifice results in complex spatial and temporal variations in deformation kinematics. While this makes the recognition, assessment, and monitoring of volcano slope instability challenging, advancements in Synthetic Aperture Radar (SAR) technology have significantly accelerated our knowledge of instability phenomena and our ability to assess their hazards.

This review discusses the applications and challenges of SAR imagery to various slope instabilities at volcanoes around the world. SAR amplitude images are powerful tools for mapping areas of geomorphological changes. These snapshots can be combined using Interferometric SAR (InSAR) to create multi-temporal deformation maps that provide unique information on the evolution of slope failures. Space-borne InSAR has become an economic way to detect changes at volcanoes at very high resolution. Ground-Based InSAR (GBInSAR) can produce frequent SAR images (on the order of seconds to minutes), propelling InSAR from monitoring to surveillance and early-warning applications. However, interpreting InSAR-derived ground deformation signals related to volcano slope instability is still challenging. Deformation from magma rise or variations in hydrothermal systems may be inseparable from persistent, deep-seated flank motion. Similarly, shallow or localized ground motion may occur in overlap with thermal contraction or subsidence of newly emplaced lava or tephra deposits.

If triggered to failure, landslides can vary over several magnitudes, from small-volume rock falls that pose only a localized hazard, to large-volume debris avalanches capable of travelling tens of kilometers away from the source. These collapses can have cascading hazards if accompanied by directed blasts or tsunamis, emphasizing the need for continued advancement of our understanding of these events and their consequences. To highlight the utility of SAR for measuring and monitoring mass movement, two case studies of Stromboli (Italy) and Pacaya (Guatemala) volcanoes are discussed in detail, where recent instability events, persistent volcanic activity, and ground truth constraints have resulted in excellent case-histories in applying SAR imagery to understand these potentially hazardous slope instabilities.

## 1. Introduction

Recent geomorphic and deformation studies, and evidence from historic and geologic records, emphasize both the widespread past occurrence and potential of structural failure at volcanoes. Collapses have

occurred on all types of volcanoes, in all states of activity or dormancy, and in all geodynamic contexts (Ui, 1983; Siebert, 1984; McGuire, 1996; Voight and Elsworth, 1997; Voight, 2000; Shea and Van Wyk De Vries, 2010; de Vries and Davies, 2015). Volcanoes produce a wide spectrum of instability phenomena, from small-scale rockfalls to large

\* Corresponding author at: Dipartimento di Scienze della Terra, Università degli Studi di Firenze, Via La Pira, 4, 50121 Florence, Italy.  
E-mail address: [federico.ditraglia@unifi.it](mailto:federico.ditraglia@unifi.it) (F. Di Traglia).

scale slope deformation, which can evolve into potentially deadly rock-slides or debris avalanches (Siebert et al., 1987; Siebert, 1996; Carrasco-Núñez et al., 2011).

Due to their complex nature, successful strategies for volcano slope instability hazard assessments involve integrated methodologies for detection, mapping, and monitoring. This often requires the combined use of field-based studies and geomorphological mapping with remote sensing, geophysical and geochemical investigations, and/or numerical modeling. Geodetic techniques are particularly useful for determining the extent and current state of volcano slope instability, with many benefits arising from the use of synthetic aperture radar (SAR) data (Ebmeier et al., 2010; Bonforte and Guglielmino, 2015; Froger et al., 2015; Schaefer et al., 2015a; Di Traglia et al., 2018c). Tracking surface deformation using the phase difference between two space-born SAR images (differential interferometric SAR, denoted as DInSAR or InSAR; Massonnet and Feigl, 1998) permits the remote detection of centimeter-scale displacements of large areas of the Earth's surface along the satellite line of sight (LOS) direction (Hu et al., 2014). InSAR has been used extensively to measure displacements associated with earthquakes, volcanic activity, and other ground deformation (Chaussard et al., 2013a; Chaussard et al., 2013b; Pinel et al., 2014; Chaussard et al., 2015; Ciampalini et al., 2015; Elliott et al., 2016; Chaussard et al., 2017; Dumont et al., 2018; Garthwaite et al., 2018).

While a two-image approach can measure centimeter-scale displacements, processing a long stack of images using multi temporal (MT) InSAR techniques allows for the detection of millimeter-scale displacements over long time frames through the reduction of error sources (Ferretti et al., 2001; Berardino et al., 2002; Hooper, 2008; Ferretti et al., 2011; Crosetto et al., 2016). Two common MTInSAR methods include persistent or permanent scatterer InSAR (referred to as PS, PSInSAR, or PSI) and small baseline subset (SBAS) methods. PSI identifies coherent or 'stable' reflectors (permanent scatterers) typically smaller than the resolution cell over long time intervals, which maximizes the signal to clutter ratio of resolution cells. SBAS methods uses interferograms with perpendicular baseline (offset between satellite orbit tracks) values below a threshold to limit geometric decorrelation. Detecting subtle volcano slope movements through PSI can provide unique information on the spatial and temporal evolution of slope failures. Ground-Based InSAR (GBInSAR) has the additional advantage of producing frequent SAR images (on the order of seconds to minutes), resulting in very high frequency slope maps and time series. With these fast repeat time intervals, GBInSAR has led InSAR from mapping to surveillance and early-warning applications (Di Traglia et al., 2014b; Carlà et al., 2016a; Carlà et al., 2016b; Kuraoka et al., 2018). Moreover, the use of GBInSAR in the Ku-band (17–17.1 mm radar) can penetrate dust clouds (abundant especially during collapse events), and will work in variable light and atmospheric conditions (Calvari et al., 2016).

In volcanic environments, corrections are often required to account for the variability of tropospheric water vapor (e.g. Williams et al., 1998; Wedge et al., 2002; Peltier et al., 2010; Welch and Schmidt, 2017; Di Traglia et al., 2018c). Even with advanced processing techniques, there undoubtedly remains difficulties in interpreting ground deformation signals and separating instability-related movements from other volcanic phenomena. Persistent, deep-seated flank motions (e.g. Borgia et al., 1992; Lundgren and Rosen, 2003; Lundgren et al., 2004; Poland et al., 2017) can affect a large part of a volcano (reaching as deep as the substrata; de Vries and Davies, 2015), but the deformation signal may be overprinted by large-scale deformation due to inflation or deflation of deep magma sources (e.g. Lanari et al., 1998; Lundgren et al., 2004; Lu and Dzurisin, 2010). Similarly, localized motion can occur in tandem with changes in the magma system (Nolesini et al., 2013; Schaefer et al., 2015a; Schaefer et al., 2016; Schaefer et al., 2017; Wnuk and Wauthier, 2017), potentially leading to signal overlap. Even instability of shallow surface deposits (Ebmeier et al., 2014) can be difficult to separate from other superficial, non-instability related deformation such as thermal contraction, compaction, or loading of lava

flows or other deposits (Stevens et al., 2001; Masterlark et al., 2006; Odber et al., 2015; Chaussard, 2016; McAlpin et al., 2016).

Beyond the challenges associated with SAR processing and interpretation, the key challenges for volcano slope instability studies related to hazard management are: (1) How do we cope with persistent, steady state flank dynamics such as creep (flank spreading) and/or shallow slope processes (material erosion and remobilization)? And; (2) In the case of onset of flank acceleration ("flank unrest") due to magmatic intrusion, tectonic activity, hydrothermal fluids circulation, how can ground deformation monitoring or modeling be used in emergency planning?

In this paper, the diversity of slope instability and the applications and challenges of using SAR-derived products for the identification, mapping, and forecasting of these mass movements are reviewed. To emphasize the potential utility of SAR, we highlight the case-studies of Pacaya (Guatemala) and Stromboli (Italy) volcanoes, as: (1) they recently experienced moderate to major instability events; (2) their slopes are prone to landsliding; (3) the volcanoes are persistently active, which influences their stability; (4) landslides from their flank could directly (debris avalanche at Pacaya; Sosio et al., 2012) or indirectly (tsunamis at Stromboli; Tinti et al., 2006b) affect populated areas, and; (5) a variety of SAR techniques were applied for each case study.

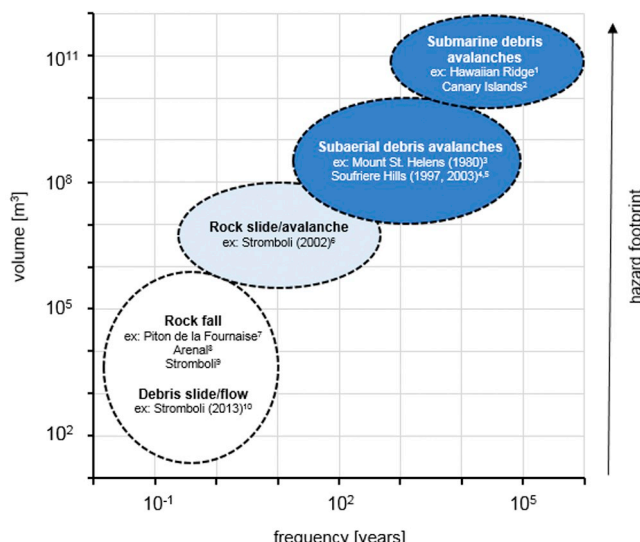
## 2. The diversity of volcano slope instability and related hazards

In this paper, we concentrate on examples of lateral (flank/slope) movement of volcanic edifices. This excludes vertical (caldera, pit craters) collapses, which are largely driven by depletion of a buoyant magma source (Kennedy et al., 2017), although studies have shown that vertical collapses can trigger large lateral landslides of the caldera margins (Martí et al., 1997), and can be associated with lateral propagation of dikes, triggering flank movements (Owen et al., 1995; Di Traglia et al., 2014c).

Defining the characteristics and dynamics of volcanic slope instability is critical for assessing the frequency, magnitude, and mobility of mass movement hazards. If material is triggered to collapse/failure (i.e. loss of shear strength leading to rapid and short-lived slides, flows, or avalanches), the implications of a given event depend on the type of material involved, the topography, and the velocity and spatial extent (i.e. magnitude) of the landslide, among other factors. Different volcano slope instability phenomena and their characteristic volume ranges are shown in Fig. 1, and examples of the spatial extent of landslide source areas at various volcanoes are shown in Fig. 2. In general, surficial mass movements such as gravel slides or rock falls tend to be more frequent (days-years), have a smaller volume ( $< 10^6 \text{ m}^3$ ), and a smaller hazard footprint. Larger mass movements ( $> 10^6 \text{ m}^3$ ) such as rock slides or debris avalanches typically have deeper-seated failure planes and incorporate larger portions of a volcanic flank and even parts of the magmatic or hydrothermal system. While less frequent (tens to hundreds of years), they can travel longer distances, resulting in larger hazard footprints. The largest of these events ( $> 10^{10} \text{ m}^3$ ) are much less frequent (tens to hundreds of thousands of years) (McGuire, 1996). These massive structural instabilities are typically characteristic of major continental or oceanic polygenetic volcanoes that have greater volumes; the largest known "megaslides" (in excess of  $5 \times 10^{12} \text{ m}^3$ ) have originated from ocean-island volcanoes (Carracedo, 1994; Moore et al., 1994; Poland et al., 2017; Blahut et al., 2018; Paris et al., 2018).

The conditions and triggers for failures at volcanoes have been widely discussed, including composition (e.g. Voight and Elsworth, 1997; Voight, 2000) and structure (e.g. Carrasco-Núñez et al., 2006), gravitational forces (e.g. de Vries and Davies, 2015), hydrothermal alteration (e.g. Reid et al., 2001), fluid-rock interactions (e.g. Rasà, 1991; Bonaccorso et al., 2010), magmatic and phreatic activity (e.g. Siebert et al., 1987), pore fluid pressures (e.g. Day, 1996), erosion (e.g. Ramalho et al., 2013), tectonics (e.g. Tibaldi et al., 2006), earthquake shaking (e.g. Hildenbrand et al., 2018; Keating and McGuire, 2000),

(A)



(B)

Category	Volume	Description
Deep-seated slope deformations evolving into debris avalanches	> 10⁷ m³	Large-scale deformation of an unstable volcano flank, manifested by scarps, benches, cracks, trenches and bulges, but may lack a fully defined rupture surface. Evolving into extremely rapid, massive, flow-like motion of fragmented rock and volcaniclastics.
Rock (rotational or planar) slide evolving into rock avalanches	= 10⁶ - 10⁸ m³	Sliding of a mass of rock on a rotational or planar rupture surface that is not structurally controlled. Evolving into extremely rapid, massive, flow-like motion of fragmented rock.
Rock fall evolving into dry gravel/debris flows	< 10⁶ m³ (typically < 10⁵ m³)	Detachment, fall, rolling, and bouncing of rock. Evolving into (generally) rapid flow-like movement of loose, dry, sorted or unsorted granular material, and without excess pore pressure.
Gravel/debris slide evolving into dry gravel/debris flows	< 10⁶ m³ (typically < 10⁵ m³)	Sliding of a mass of granular material on a shallow, planar surface. Evolving into (generally) rapid flow-like movement of loose dry, sorted or unsorted granular material, and without excess pore pressure.

**Fig. 1.** Summary of the range of mass movements on volcanoes. (A) Frequency/magnitude chart modified from McGuire (1996). References: (1) Moore et al. (1994); (2) Carracedo et al. (1999); (3) Voight et al. (1983); (4) Voight et al. (2002); (5) Herd et al. (2005); (6) Chiocci et al. (2008); (7) Hibert et al. (2017); (8) Ebmeier et al. (2014); (9) Di Traglia et al. (2018c); (10) Calvari et al. (2016). (B) Descriptions and characteristic volume ranges of different volcano slope instability phenomena. Terminology based on classifications from Hungri et al. (2014).

and climatic changes (e.g. Capra, 2006; Roberti et al., 2018). In simplified terms, failures controlled by shear forces (e.g. slides) can be considered to have a limit equilibrium condition, i.e. a unity ratio (namely factor of safety;  $F$ ), between the shear stress ( $\tau$ ) and the shear strength ( $s$ ):

$$F = \frac{s}{\tau} \quad (1)$$

with shear strength defined by the Coulomb-Terzaghi failure rule,

$$s = c + (\sigma_n - u) \tan\varphi \quad (2)$$

where  $c$  is cohesion,  $\sigma_n$  is the normal stress,  $u$  is the pore-water pressure acting on the shear surface, and  $\varphi$  is the angle of internal friction. An increase in the shear stress (e.g. slope over-steepening, dynamic loading from dike intrusion or seismic shaking) or a reduction in the shear strength (e.g. hydrothermal alteration, increase in pore fluid pressure) can lead to a sudden drop in  $F$  and acceleration of the flank (Voight and Elsworth, 1997; Reid et al., 2000; Reid et al., 2001; Reid, 2004; Apuaní

et al., 2005; Reid et al., 2010; Schaefer et al., 2013).

Alternatively, the potential for tensional failures (e.g. toppling in lava domes) is often estimated using the following kinematic condition from Goodman and Bray (1976):

$$(90 - \delta) + \varphi < \alpha \quad (3)$$

where  $\alpha$  is the inclination of the face slope,  $\varphi$  is the friction angle between the layers, and  $\delta$  is the inclination of the layers. This condition has been incorporated into equilibrium equations for flexural toppling (e.g. Amini et al., 2009).

Models of slope stability require reliable estimates of physical and mechanical material properties. This can be challenging in volcanic environments, where material is microscopically and macroscopically heterogeneous, and subjected to high temperatures and varying pressures. Recent experimental rock mechanic studies have shown that the mechanical response (i.e. strength and strain) of volcanic rocks can change under volcanically relevant conditions such as thermal stressing, cyclic loading (i.e. inflation-deflation cycles by intrusions), and high temperatures (e.g. Balme et al., 2004; Kendrick et al., 2013; Heap et al., 2015; Schaefer et al., 2015b), which are important considerations for stability modeling or interpreting measured displacements.

Slope instability can be hazardous to humans and the environment, either directly from falls, flows, and avalanches, or through secondary (cascading) hazards like tsunamis and lahars (Siebert, 1984; Major et al., 2000). Volcanic landslides may depressurize the hydrothermal and/or magmatic system, triggering violent lateral eruptions (i.e. Siebert et al., 1987; Belousov et al., 2007). If the landslides enter bodies of water, they can also generate tsunamis (Ward and Day, 2003; Tinti et al., 2006a). Large-scale gravitational flank collapses are thought to be capable of generating megatsunamis with run-up heights of hundreds of meters (i.e. Ramalho et al., 2015), although recently, some giant landslides previously thought to be single large debris avalanches have been reinterpreted as multistage failures (Hunt and Jarvis, 2017; Hunt et al., 2018).

### 3. Volcano slope failures around the world

The landslide that initiated the 1980 eruption at Mount St Helens (Lipman and Mullineaux, 1981) was the first to be monitored in detail from slope deformation through to failure, prompting numerous investigations into the characteristics and global frequency of large volcanic slope failures (e.g. Ui, 1983; Siebert, 1984; Siebert et al., 1987). Regional surveys of debris-avalanche deposits have since been conducted for the West Indies (Roobol et al., 1983), Kamchatka (Melekestsev and Braitseva, 1984; Leonov, 1995), Japan (Ui et al., 1986), Melanesia (Johnson, 1987; Silver et al., 2009), South America (Francis and Wells, 1988; Schuster et al., 2002), Indonesia (MacLeod, 1989), New Zealand (Palmer et al., 1991), the Canary Islands (Carracedo, 1994), and Central America (Vallance et al., 1995; Carrasco-Núñez et al., 2006; Siebert et al., 2006), in addition to many individual volcano studies. While large-scale volcanic edifice collapse has been identified at > 400 Quaternary volcanoes worldwide (Siebert et al., 2006), several studies have also revealed the tendency for volcanoes to collapse repeatedly in their lifetime. Mt. Taranaki in New Zealand, for example, has had 14 major (1 to > 7.5 km³) and four smaller (0.1 to 0.2 km³) collapses (Neall, 1979; Alloway et al., 2005; Zernack et al., 2011). Although these frequencies are not typical, repetitive failure is possible at volcanoes with persistent magmatic activity or in active tectonic settings (i.e. Kilauea volcano, Hawaii; Poland et al., 2017), or high magma extrusion rates that rapidly reconstruct the edifice (i.e. Mount St. Augustine volcano in Alaska with 11 major collapses Begét and Kienle, 1992). Thus, estimates by Siebert (1984) of a global frequency of 4 large-scale edifice failures per century, are likely conservative.

In the last 150 years, there have been 12 large-volume collapse events (0.05 km³ or larger) that have resulted in debris avalanches,

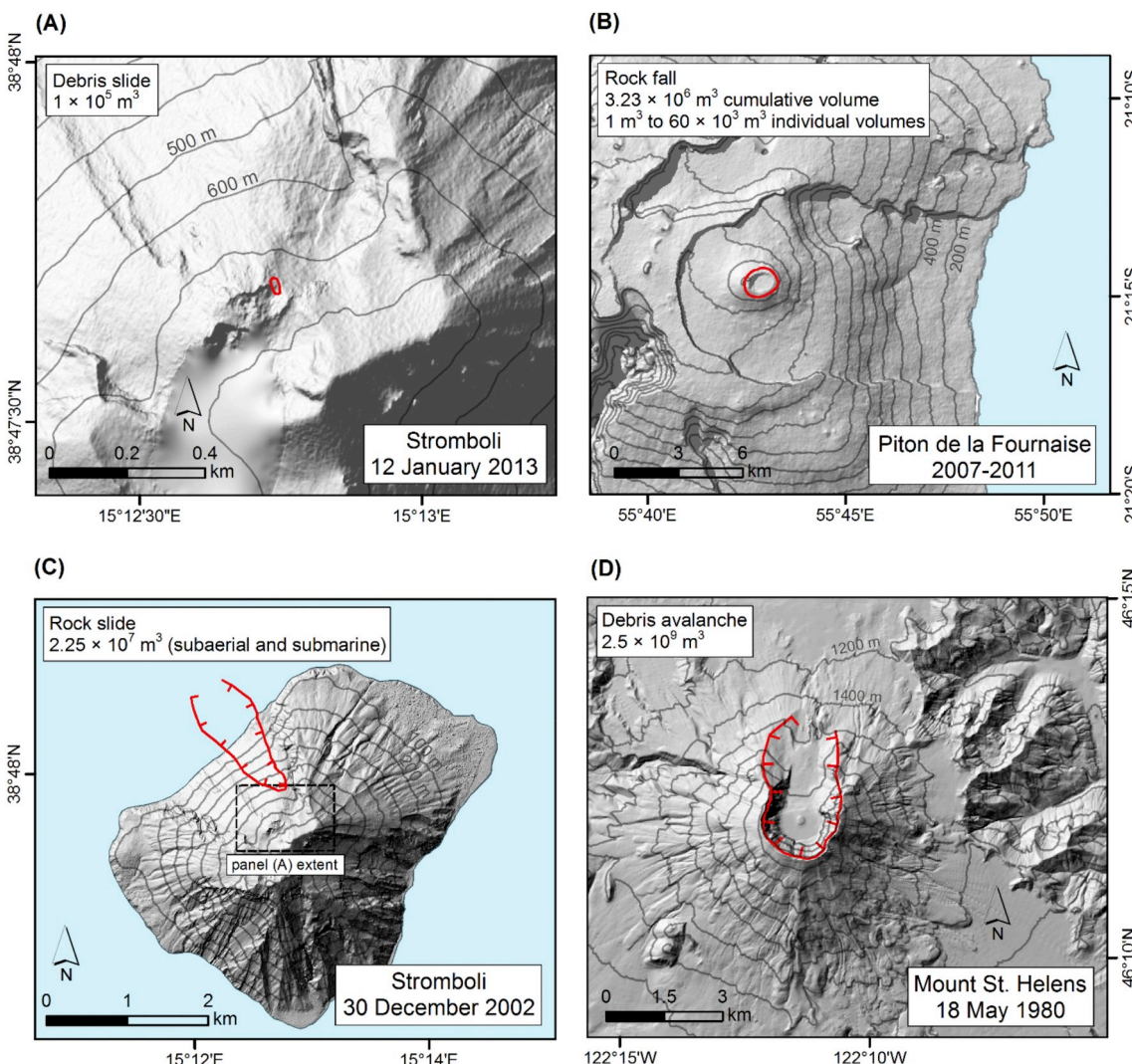


**Fig. 2.** Spatial extent of various volcanic landslide source areas. Source areas are outlined in red, and approximate extent of volcanic edifices are outlined in black. (A)  $1 \times 10^5 \text{ m}^3$  debris slide, Stromboli (Italy) 12 January 2013 (Calvari et al., 2016). (B)  $3.23 \times 10^6 \text{ m}^3$  (cumulative volume) rock fall, Piton de la Fournaise (Réunion Island) 2007–2011 (Hibert et al., 2017). (C)  $2.25 \times 10^7 \text{ m}^3$  rock slide, Stromboli (Italy) 30 December 2002 (Chiocci et al., 2008). Dashed box indicates extent of Fig. 2A. (D)  $2.5 \times 10^9 \text{ m}^3$  debris avalanche, Mount St. Helens (Cascades, USA) 18 May 1980 (Voight et al., 1983). While in general the resulting hazard footprint increases with initial amount of failed material, the outlined source areas do not necessarily indicate the resulting hazard footprint (i.e. due to landslide runout). For example, the 2002 Stromboli rock slide (Fig. 2c) created a tsunami that had a measurable impact as far as the Sicily coast c. 70 km away. Likewise, the Mount St. Helens debris avalanche covered an area of  $64 \text{ km}^2$  ( $26 \times 0.5\text{--}5 \text{ km}$ ) to the north, with the longest travel path being 29 km from the source, and was accompanied by a lateral blast, pyroclastic flows, and lahars (Glicken, 1996). (For interpretation of the references to color in this figure legend, the reader is referred to the web version of this article.)

**Table 1**

Known large-volume volcano collapse events ( $0.05 \text{ km}^3$  or larger) in the last 150 years, expanded from Siebert (1996) and Carrasco-Núñez et al. (2011).

Volcano	Location	Date	Volume ( $\text{km}^3$ )
Mount Meager	Canada	2009	0.05
Soufrière Hills	Montserrat	2003	0.21
Soufrière Hills	Montserrat	1997	0.05
Fernandina	Galapagos	1988	0.9
Mount St. Helens	Cascades	1980	2.5
Ili Werung	Indonesia	1979	0.05
Shiveluch	Kamchatka	1964	1.5
Bezymianny	Kamchatka	1956	0.8
Kharimkotan	Kurile Islands	1933	0.5
Mageik	Alaska	1912	0.1(?)
Bandai	Japan	1888	1.5
Ritter Island	Melanesia	1888	5
Augustine	Alaska	1883	0.3

debris flows and/or tsunami, emphasizing the widespread occurrence of volcanic mass movements (Table 1, Fig. 3). Additional notable collapse events have recently occurred at Casita Volcano, Nicaragua in 1998 ( $1.6 \times 10^6 \text{ m}^3$  precipitation-triggered flank collapse, Kerle, 2002), TeMaari crater of Mt. Tongariro, New Zealand in 2012 ( $7.74 \times 10^5 \text{ m}^3$  debris flow, Procter et al., 2014), Askja caldera, Iceland in 2014 ( $20 \times 10^6 \text{ m}^3$  rockslide, Gylfadóttir et al., 2017), and Soufrière Hills Volcano, Montserrat in 2000 ( $46 \times 10^6 \text{ m}^3$  debris avalanche, Sparks et al., 2002).

In the last 400 years, major slope failures are thought to have caused 20,000 fatalities (Siebert, 1984). While large failures are more easily recognized in the geologic record and thus more likely to be recorded in historic accounts, even small collapses can have severe consequences. For example, the 18 March 2007 dam-break collapse on the order of  $100 \text{ m}^3$  at the crater rim of Mt. Ruapehu volcano (New Zealand) released  $1.8 \times 10^6 \text{ m}^3$  of water from the crater lake. This generated a lahar that destroyed a railway bridge, causing an oncoming express

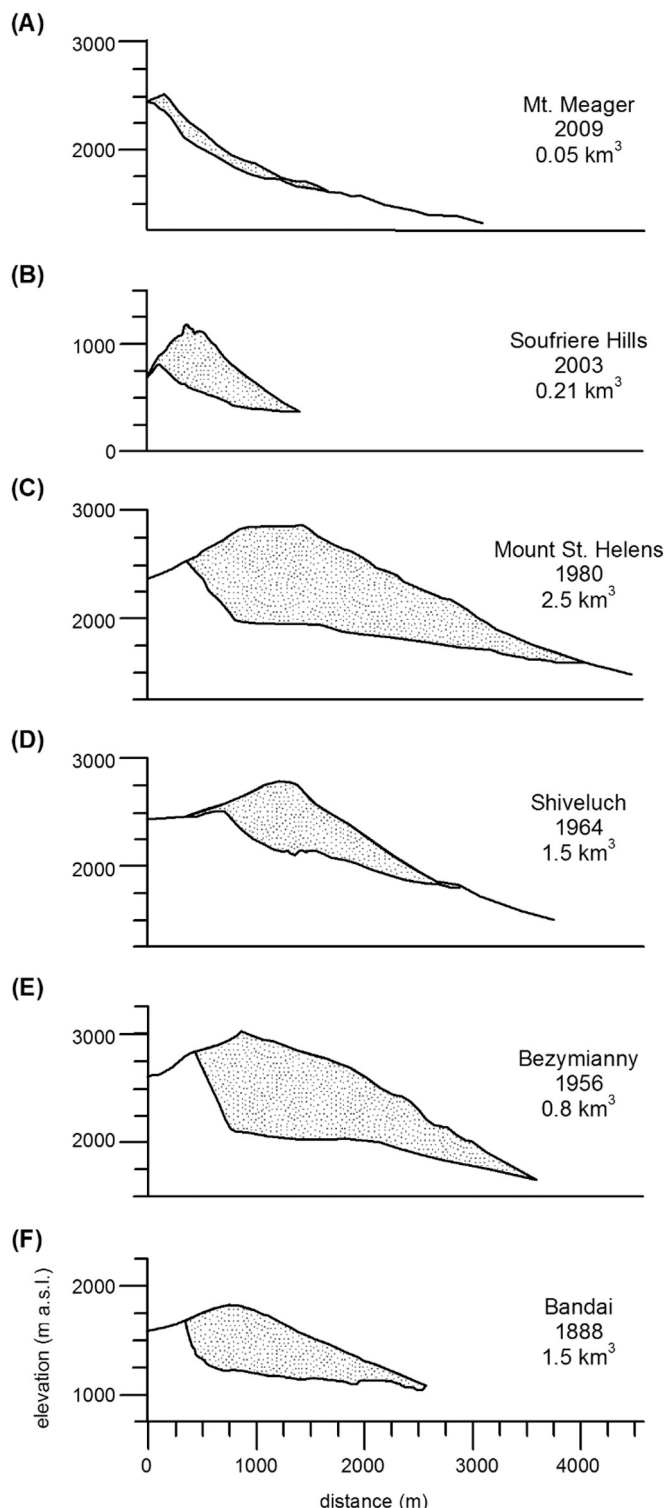


**Fig. 3.** Examples of collapse profiles of large-volume ( $0.05 \text{ km}^3$  or larger) volcanic landslide events in the last 150 years. (A) Mt. Meager (Canada) profile from [Guthrie et al. \(2012\)](#); (B) Soufriere Hills (Montserrat) profile from [Herd et al. \(2005\)](#); (C) Mount St. Helens (USA) from [Glicken \(1996\)](#); (D) Shiveluch (Kamchatka) profile from [Ponomareva et al. \(1998\)](#); (E) Bezymianny (Kamchatka) profile from [Siebert \(1984\)](#); (F) Bandai (Japan) profile from [Sekiya and Kikuchi \(1889\)](#). Figure modified from [Siebert \(1984\)](#).

train to fall off the destroyed bridge and into the river, killing 151 people (Tangiwai disaster; [O'Shea, 1954](#)). Small dome collapses can also become deadly events if they generate pyroclastic flows, such as

the generation of pyroclastic flows at Unzen volcano in 1992 due to rock fall from the crumbling Fugendake dome, one of which killed 43 people ([Sato et al., 1992](#)).

#### 4. Measuring and monitoring volcano slope instability with SAR and other geodetic methods

Geodetic measurements have allowed for quantitative evaluations of recent or ongoing volcanic slope movement using techniques such as GPS (e.g. [Borgia and de Vries, 2003](#); [Clarke et al., 2013](#)), precision leveling (e.g. [Murray and Wooller, 2002](#); [Acocella et al., 2003](#)) and trilateration and tilt (e.g. [Delaney and Denlinger, 1999](#); [Murray and Wooller, 2002](#)). Since the launch of the ERS-1, JERS-1, RADARSAT-1, and ERS-2 SAR satellites in the 1990's, followed by ENVISAT, RADARSAT-2, ALOS-1 and -2, TerraSAR-X, COSMO-SkyMed, SENTINEL-1A/B, and the NASA UAVSAR airborne system, in the first two decades of the 21st century, SAR has been used to make measurements of instability around the world (see Fig. 4, Table 2 for examples). Unique from other geodetic methods, satellite remote sensing allows for the measurement of a continuous deformation field over the full spatial extent of a volcano, which can reveal unique details about displacement variations over the length of a given landslide (e.g. [Schaefer et al., 2017](#)).

The recent development of GBInSAR systems now allows for near continuous observations of displacement measurements and topographic changes, revealing unprecedented temporal detail of volcanic activity at Stromboli ([Antonello et al., 2004](#); [Bonforte et al., 2008](#); [Tarchi et al., 2008](#); [Casagli et al., 2009](#); [Di Traglia et al., 2013](#); [Intrieri et al., 2013](#); [Nolesini et al., 2013](#); [Di Traglia et al., 2014a,b,c, 2015, 2018c](#)), Soufrière Hills ([Wadge et al., 2005, 2008](#)), and Arenal ([Macfarlane et al., 2006](#)). Measurements of current or recent volcano slope instability using various geodetic techniques are given in Table 2.

For the purposes of measuring and monitoring volcano slope instability with SAR, we can group slope instability phenomena as follows:

- (1) *Deep-seated, persistent flank motion* (i.e. flank spreading or sagging; [de Vries and Davies, 2015](#)): typically deep-seated, steady-state movement of large sectors of a volcanic edifice due to gravity (i.e. edifice compaction, basal décollement sliding, or substrate flow) or regional tectonics ([Borgia et al., 1992](#); [Merle and Borgia, 1996](#); [De Vries and Francis, 1997](#); [de Vries and Davies, 2015](#); [Poland et al., 2017](#)). It is generally thought that volcanoes with persistent flank motion are less likely to suffer large-volume landslides because elastic stress can be relaxed due to the very slow deformation rate, reducing the development of normal faults that can be exploited as slip surfaces ([De Vries and Borgia, 1996](#)). However, a sudden trigger to failure through rapid flank detachment or volcano-base ment de-coupling is possible, especially if spreading occurs in a single direction ([Borgia and de Vries, 2003](#)). Alternatively, a sector could detach and continue to slide under gravity for tens of thousands of years (e.g. Mt. Etna; [Borgia et al., 1992](#); [Gross et al., 2016](#); [Urlaub et al., 2018](#)). Persistent flank motion can be very slow, on the order of mm's a year. Because of increasing incoherence over these long time frames, these slow movements can typically only be measured using MTInSAR techniques such as persistent scatterer or small baselines (e.g. [Hooper, 2008](#)). Relatively low temporal resolution monitoring (c. once a month) is typically acceptable, although changes in persistent or steady-state movement, or periods of increased eruptive activity, should be carefully monitored.
- (2) *Deep-seated, transient flank motion* (i.e. flank "unrest"; [Acocella and Puglisi, 2013](#)) is associated with intrusive processes ([Casagli et al., 2009](#); [Bonforte and Guglielmino, 2015](#); [González et al., 2015](#)), co-eruptive deformation ([Froger et al., 2015](#); [Schaefer et al., 2015a](#)), seismic shaking ([Owen and Bürgmann, 2006](#); [Chen et al., 2019](#)), lava dome growth ([Calder et al., 2002](#)), or other relatively rapid

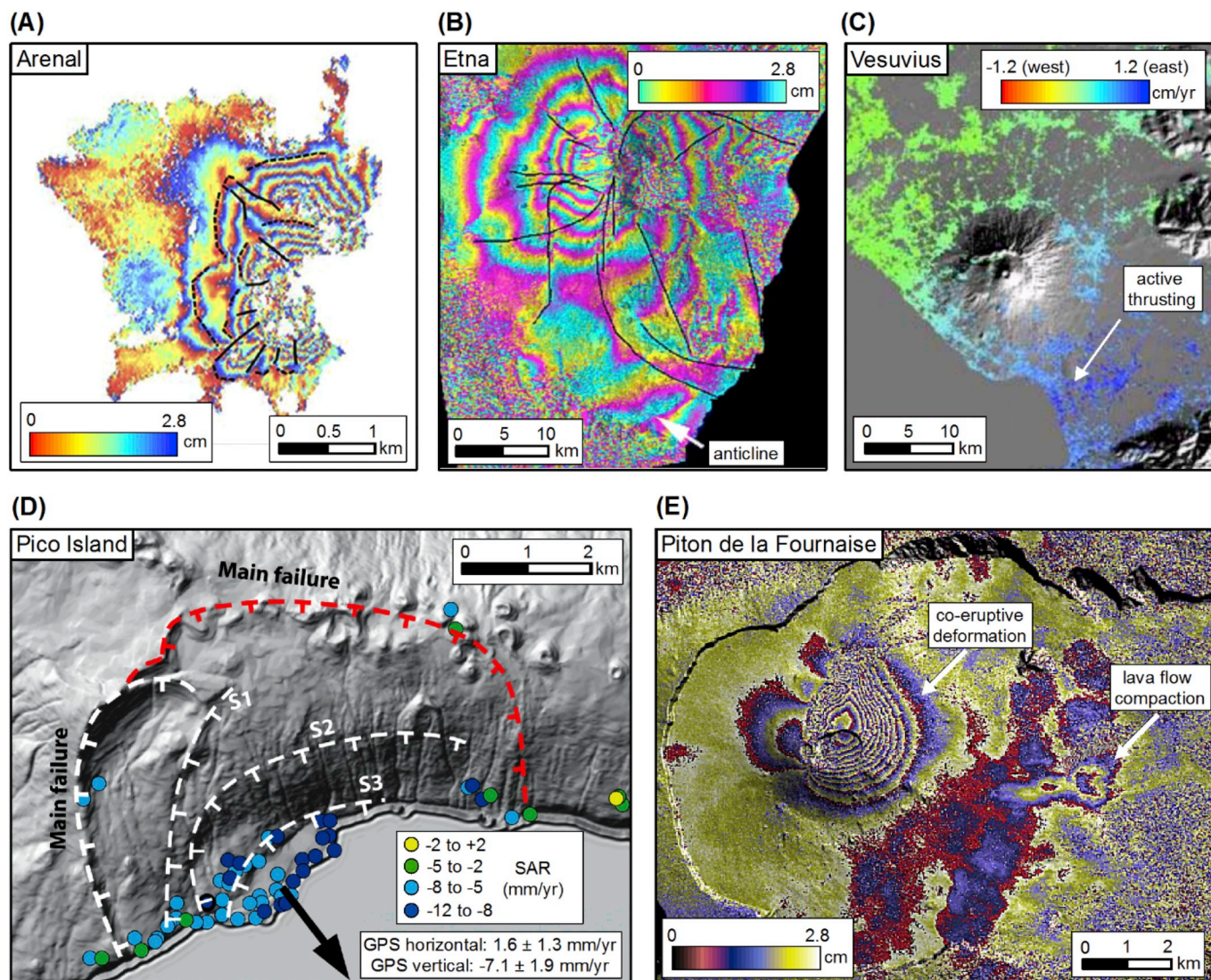


**Fig. 4.** Examples of slope instability measured with SAR techniques. (A) Mass wasting at Arenal volcano (Costa Rica) from Ebmeier et al. (2014). Solid black lines indicate boundaries of different sliding units, while dashed black line indicates the extent (toe) of the sliding units; (B) Spreading of Etna volcano (Italy) from Lundgren et al. (2004). Arrow points to anticline growth, which is evidence of volcano spreading driven by deeper magma injection at depth; (C) Gravitational spreading at Vesuvius volcano (Italy) from Borgia et al. (2005). Map shows general regional displacement trends, with the arrow pointing to an area of slightly higher values of eastward displacement from the area just to the south, indicative of active thrusting due to volcanic spreading; (D) Gravitational creep at Pico Island (Azores) from Hildenbrand et al. (2012). Black arrow indicates horizontal GPS motion, and colored circles indicate average vertical SAR displacements in mm/yr (negative values for downward movement and positive values for upward movement) for the given time period. S1, S2, and S3 indicate different scarps within the main failure complex; (E) Transient slope motion (due to dike intrusion) at Piton de la Fournaise (Réunion Island) from Froger et al. (2004). Arrows point to co-eruptive (eastward) deformation and recent lava flow compaction.

increases in shear stress (Voight and Elsworth, 1997). Transient flank motion may be a precursor to catastrophic (i.e. rapid onset, long runout) sector collapses (Lipman and Mullineaux, 1981; Voight et al., 2002). However, there have been cases of very large, rapid-onset flank movements that arrested during the early stages of sliding (e.g. Carracedo et al., 1999; Schaefer et al., 2015a). Transient movement is typically fast (order of hours to months), with high magnitude displacements (10's to 100's of cm's), and higher likelihood of failure.

Given these characteristics, an ideal SAR monitoring system needs to be accessed or implemented quickly, have a high temporal resolution, and ideally have longer wavelengths (e.g. L-band around 24 cm vs. C-band around 6 cm) to resolve the relatively large yet short-lived displacements. Tasked deployment missions through aircraft-based sensors such as the NASA Uninhabited Aerial SAR (UAVSAR), operated

by the Jet Propulsion Laboratory (JPL), L-band sensor is one example of a high-resolution (~2 m pixel size) airborne radar system with the potential for emergency response. Very large displacements (order of meters) have been successfully measured using SAR amplitude images and pixel offset tracking techniques (e.g. Schaefer et al., 2017), and multiple-aperture interferometry (MAI) techniques (e.g. Jung et al., 2011).

(3) *Surficial flank motion (persistent or transient)* is shallow motion such as material erosion and remobilization of volcaniclastic and lava material (i.e. mass wasting; Ebmeier et al., 2014; Di Traglia et al., 2018d). Surficial flank movements are typically localized ( $\approx 10^5 \text{ m}^3$  or smaller) and very rapid (minutes to days), although smaller landslides at active volcanoes can serve as precursory activity of larger collapses (Voight et al., 2002; Di Traglia et al., 2018c). Therefore, successful SAR techniques need to have very high spatial

**Table 2**  
Measurements of current or recent volcano slope instability. Displacements indicate the maximum measured displacements over the given time frame. This list is not exhaustive, as some volcanoes have several periods or instances of flank motion (e.g. Mt. Etna; Lanari et al., 1998; Neri et al., 2009; Solaro et al., 2010), which are too detailed to be included here. Refer to individual references for details on duration, displacements, and method details. GNSS = Global Navigation Satellite System.

	Volcano	Location	Year(s)	Displacements	Deformation mechanism	Geodetic method	References
<i>Deep-seated, persistent flank motion</i>							
Concepción	Nicaragua	1994–1997	0–5 cm/yr horizontal	substrate flow	GPS	Borgia and de Vries (2003)	
Colima	Mexico	1982–1999	<7 cm/yr horizontal	edifice compaction	precision leveling and GPS	Murray and Wooller (2002)	
Cumbre Vieja	Canary Islands	1992–2000, 2003–2008	2.5 mm/yr horizontal	basal sliding	InSAR	González et al. (2010)	
Damavand	Iran	2003–2008	6 mm/yr horizontal, 5 mm/yr downward	gravitational spreading	InSAR	Shirzaei et al. (2011)	
Etna	Italy	1995–2000	c. 30 mm/yr horizontal, 10 mm/yr vertical	basal décollement and tectonic source-driven slip along basal décollement	InSAR and GPS	Bonforte et al., 2011	
Kilauea	Hawaii	1992–2001	c. 18 mm/yr horizontal	gravitational and magma (deep inflation source)-driven slip along basal décollement	InSAR	Lundgren et al. (2004)	
		2001–2012	17 mm/yr horizontal	basement sliding	GPS	Murray et al., 2018	
		1976–1996	250 cm horizontal, 200 cm vertical	gravitational and magma (deep inflation source)-driven slip along basal décollement	GPS	Delaney et al., 1998	
Mauna Loa	Hawaii	1993–1994	8 cm/yr horizontal, 8 cm/yr vertical	gravitational and magma (deep inflation source)-driven slip along basal décollement	GPS	Owen et al. (2000)	
Pico Island	Azores	2001–2009	4 cm/yr horizontal	gravitational and magma (deep inflation source)-driven slip along basal décollement	GPS	Milkilus et al. (1995)	
Piton de la Fournaise	Réunion Island	2011–2014	5–12 mm/yr downward, c. 1.6 mm/yr horizontal	lateral slumping	GNSS	Hildenbrand et al. (2012)	
Stromboli	Italy	2008–2012	c. 1.4 cm/yr horizontal	basal décollement	GNSS	Peltier et al. (2015)	
Tenerife	Canary Islands	1992–2006	0.3 cm/yr	creep	ground based InSAR	Intriieri et al. (2013)	
Vesuvius	Italy	1992–2003	3–15 mm/yr	substrate compression	InSAR and GPS	Fernández et al. (2009)	
Deep-seated, transient slope motion	Etna	2002	0.6 cm/yr downward	substrate flow	InSAR	Borgia et al. (2005)	
Kilauea	Hawaii	2011, 2012	48 cm horizontal	earthquake	trilateration	Acocella et al. (2003)	
Mount St. Helens	Cascades	1980	77 cm horizontal	co-eruptive displacement	GNSS	Poland et al. (2017)	
Pacaya	Guatemala	2010	~5 cm or less	fissure eruption, dike intrusion	triangulation, electronic distance measurement	Lipman and Mullineaux (1981)	
Piton de la Fournaise	Réunion Island	2014	150–250 cm/day horizontal	cryptodome intrusion and earthquake	PSI and InSAR	Schaefer et al. (2015a)	
		1950–2015	290–392 cm horizontal, 295 cm downward	co-eruptive displacement	InSAR	Schaefer et al. (2017)	
Stromboli	Italy	2007, 2014	?	co-eruptive displacement	photogrammetry	Wnuk and Wauthier (2017)	
Arenal	Costa Rica	2005–2009	c. 920 cm horizontal (net)	co-eruptive displacement	InSAR	Derrien et al. (2015)	
Surficial flank motion	Pacaya	2011–2013	140 cm horizontal, 33 cm downward	co-eruptive displacement	GBInSAR	Froger et al. (2015)	
Stromboli	Italy	2014	300 mm/h	co-eruptive mass-wasting	GBInSAR	Casagli et al. (2009)	
	Guatemala	2012–2014	7–10 cm/yr downslope	mass wasting, rock fall	GBInSAR	Ebmeier et al. (2010)	
	Italy	2014	–	rock fall	GBInSAR	Wnuk and Wauthier (2017)	
			70 mm/h	mass wasting	GBInSAR	Di Traglia et al. (2018a); Di Traglia et al. (2018c)	
Stromboli	Italy	2010–2016	1.6 cm/yr	submarine slope instability	GBInSAR	Di Traglia et al. (2018d)	

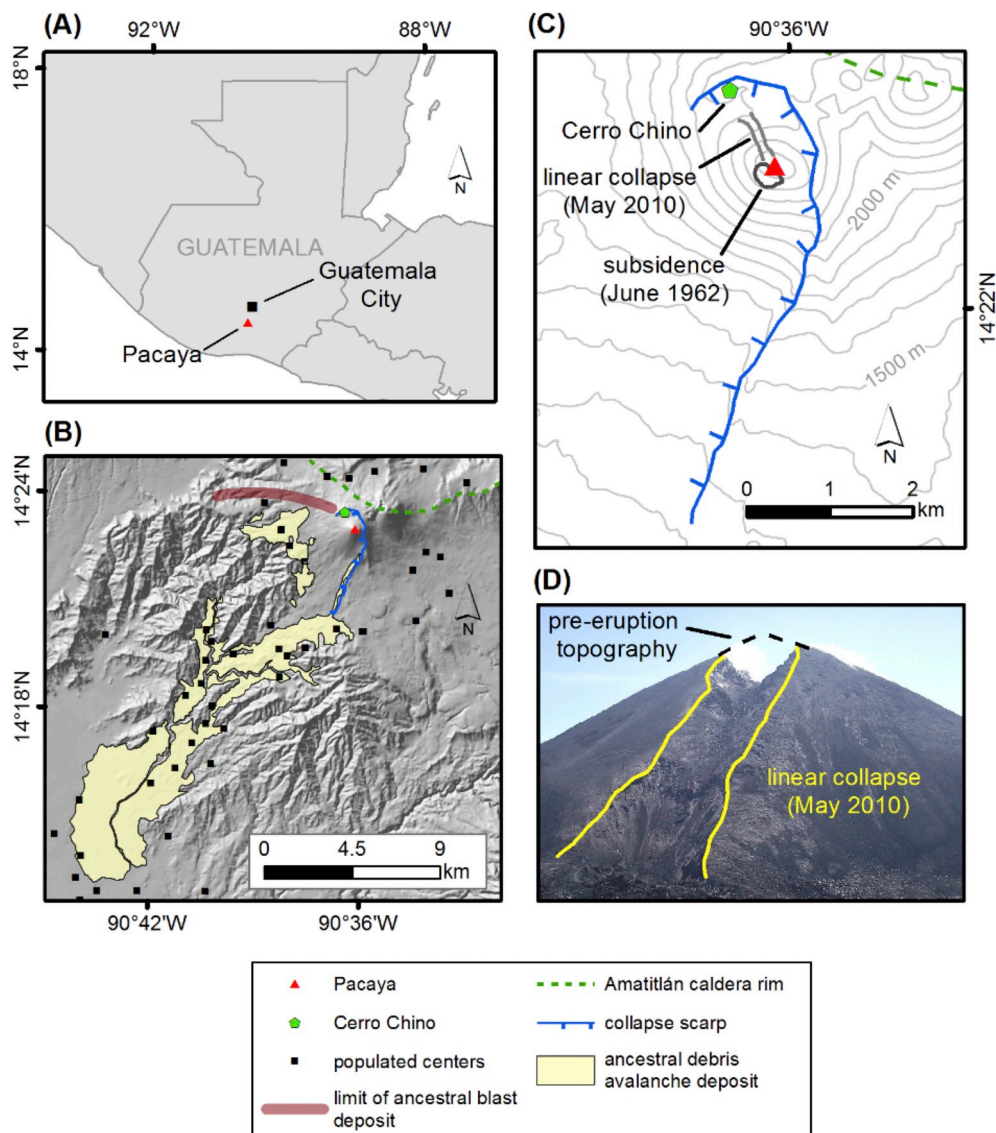


**Fig. 5.** Pacaya Volcano location, structural features, and recent collapses. (A) Pacaya Volcano is located 25 km south of Guatemala City. (B) Map showing locations of current populated centers and the extent of the debris avalanche deposit (modified from Kitamura and Matías, 1995) from the sector collapse dated between and 1500 and 600 yr B.P. The resulting collapse scarp is still visible today. (C) Recent small-scale collapses including the June 1962 subsidence and the May 2010 linear collapse. (D) Photo of the 2010 linear collapse, taken from the bottom of the collapse looking to the SE. Figure modified from Schaefer et al. (2015a).

and temporal resolution, such as GBInSAR, TerraSAR-X satellite (resolution of  $2 \times 3$  m and repeat interval of 11 days), or aerial UAVSAR. SAR amplitude images can also be used for surficial change detection, as the backscattering intensity of a given pixel will change given changes in the target area's type, shape roughness, orientation, and moisture content (e.g. Schaefer et al., 2016).

## 5. Case studies of Pacaya and Stromboli Volcanoes

### 5.1. Pacaya (Guatemala)

Pacaya is a basaltic to dacitic stratovolcano complex in Guatemala, located on the southern rim of the Amatitlán caldera 25 km south of the capital Guatemala City (Fig. 5). During an explosive phase between 1500 and 600 yr ago (Kitamura and Matías, 1995), the southwest sector of the cone failed in a major collapse, forming a  $0.65\text{--}1\text{ km}^3$  debris avalanche that traveled 25 km to the southwest (Fig. 5b; Vallance et al., 1995; Siebert et al., 2006). Episodic activity since the 16th century rebuilt the edifice within the collapse amphitheatre, creating the Cerro

Chino and modern Pacaya cone, which sit on the southern edge of the Amatitlán caldera. After a period of repose in the mid-19th century, activity renewed in 1961 with an extended period of strombolian activity and lava effusion (e.g., from 2004 to 2010; Matías Gómez et al., 2012). This activity has produced over 250 lava flows, loading the SW flank of the edifice with 100–150 m thick of primarily effusive lava. Although the volcano has grown substantially, the collapse scarp is still exposed today on the north and east sides of the cone because of asymmetric loading of material on the SW flank (Matías Gómez et al., 2012).

#### 5.1.1. Slope instability and related hazards at Pacaya

Explosive and effusive eruptions have resulted in constant morphometric changes to the edifice: in 1962, an oval-shaped area, approximately 300 by 200 m, subsided near the summit a year after a  $3.4\text{--}9 \times 10^6 \text{ m}^3$  lava flow erupted from a lower flank vent (Fig. 5c; Eggers, 1971; Matías Gómez et al., 2012). This subsidence has since been filled in by erupted material. In 2010, explosive and effusive activity on 27–28 May 2010 was accompanied by both c. 4 m of

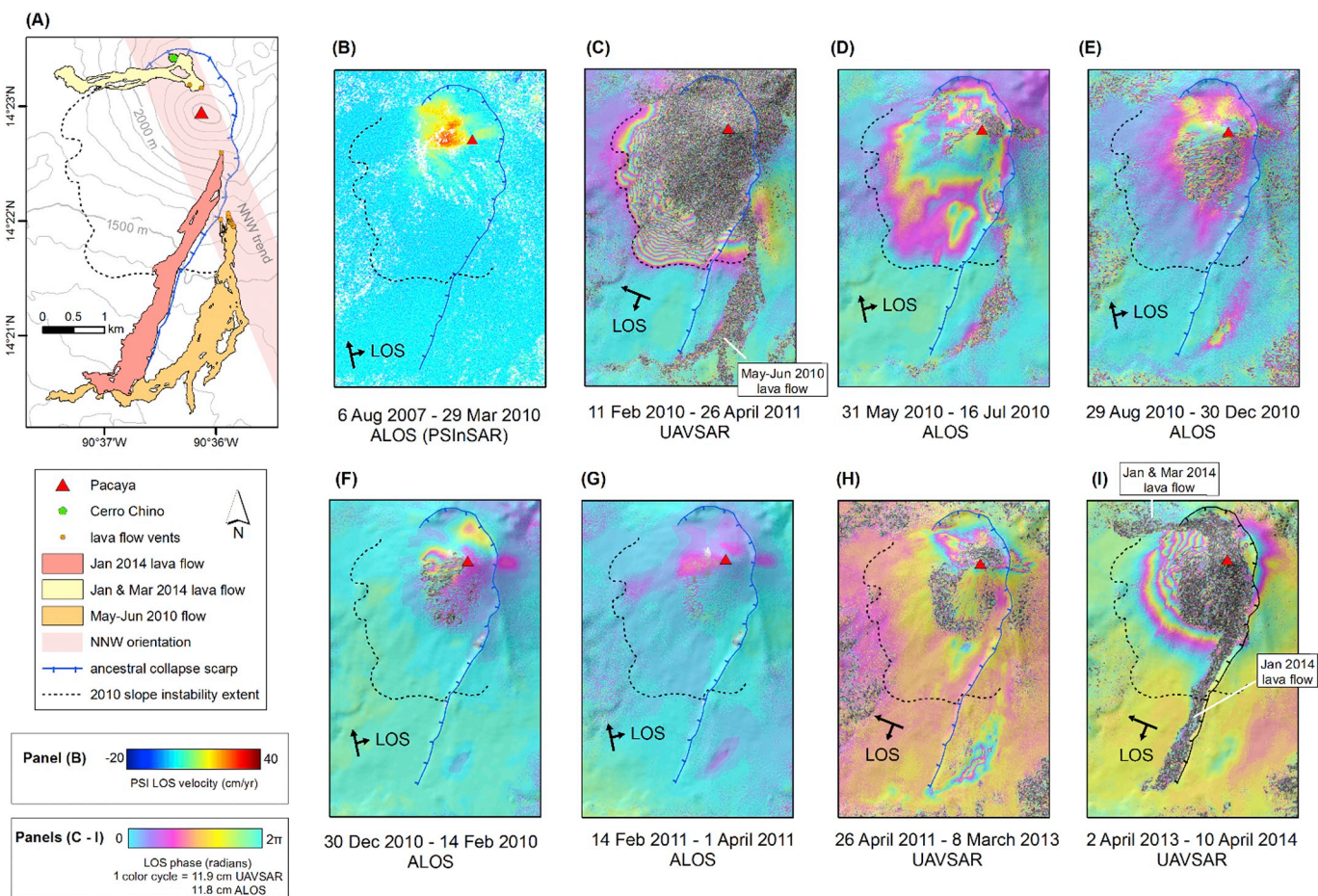


**Fig. 6.** Lava flows and radar interferometry results from 2007 to 2014, which spans both the 27 & 28 May 2010 eruption and January & March 2014 eruptions. (A) Extent of the May 2010 slope movement, ancestral collapse scarp, and lava flows that erupted beginning in May 2010, Jan 2014, and March 2014. The lava flow vents and summit crater are aligned in a NNW pattern orthogonal to the direction of flank movement, which moved to the S and SW. (B) The mean line of sight (LOS) velocity map from a PSI analysis of ALOS interferograms spanning early August 2007 to late March 2010 shows no deformation on the lower flanks. Positive LOS change corresponds to surface movement away from the satellite. Panels C–I are wrapped interferograms, with each fringe (full color cycle) representing 11.8 cm of LOS range change between the ground and the satellite for ALOS, and 11.9 cm for UAVSAR. Interferograms show the following: (C) ~270 cm of along slope (westward and downward) motion associated with the 27–28 May 2010 eruption. The edge of the slope movement coincides with the 2010 lava flow vent supporting a NNW-oriented magma intrusion, which likely provided both the “push” to destabilize the slope during its explosive phase, and the source of the later effusive phase; (D–G) Post-eruption deformation includes material settlement on the southwest flank, and cooling and subsidence of the 2010 lava flow. All displacements decrease over time, until very little displacements are measured in April of 2011; (H) Between 2 and 3 years post-2010 eruption, subsidence of the 2010 lava flow is still evident, and the elongated NW-SE subsidence remains evident near the summit; (I) During the 2014 eruptions, a maximum of ~90 cm of along-slope displacement (downward or westward) on the SW flank and ~19 cm of opposite displacement (upward or eastward) on the E flank is measured, indicating both a dike intrusion oriented NW-SE and downslope motion of the SW flank.

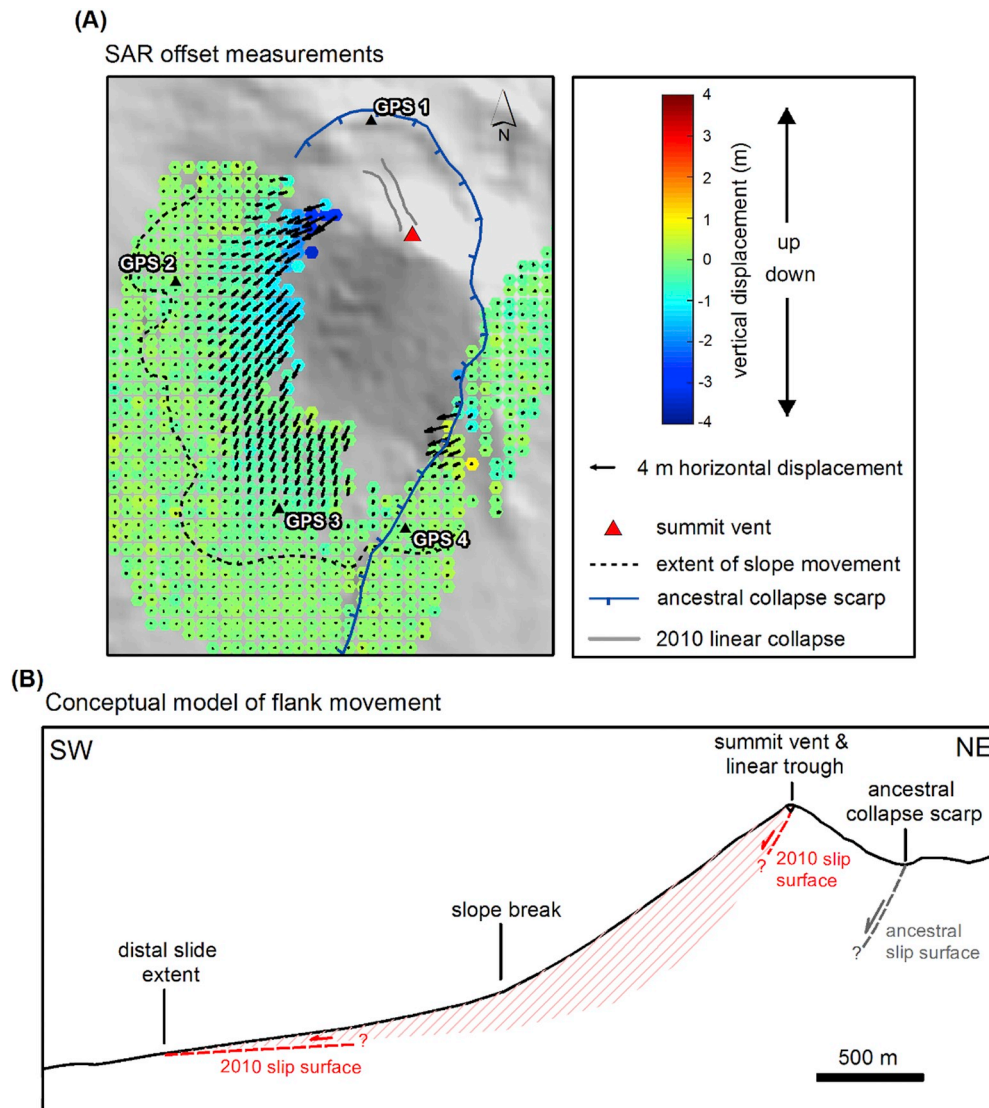
movement of the SW flank (described in Sections 5.1.2 and 5.1.3; Fig. 6), and, perhaps as a result of the flank movement, a linear collapse formed measuring 50–80 m deep and 100 m wide, and extending 600 m from the summit (collapse shown in Fig. 5c; Schaefer et al., 2013). The eruption also produced a large ( $1.6\text{--}6.4 \times 10^6 \text{ m}^3$ ) lava flow from 12 clustered lower flank vents, following a similar pattern to the lower flank lava flow-higher cone collapse in 1961/1962 (lava flow shown in Fig. 6a).

The SW flank movement is the largest slope movement detected by space and aerial geodesy to date, and suggests inherent instability of the edifice, particularly during eruptive periods. Several factors at Pacaya may also influence the stability of the edifice, including continual eruptive activity, magma storage high in the cone, high growth rates leading to over-steepening of the cone on the SW, buttressing of the edifice to the NE by other cones in the volcanic complex, a south-sloping substrate, and a tephra and ignimbrite layers deposited over the region prior to the formation of the initial cone that could remain beneath the cone (Eggers, 1983; Wunderman and Rose, 1984; Vallance et al., 1995; Matías Gómez et al., 2012; Schaefer et al., 2013).

Pacaya is surrounded by several communities totaling ~10,000 people that live within 5 km of the active cone (Fig. 5b). The dangerous proximity of these communities to the volcano is made clear by the recurrent evacuations during recent eruptions (13 evacuations since 1987, Witham, 2005; Wardman et al., 2012). Based on national census and population growth estimates from the World Bank, the hazard footprint of a debris avalanche with a magnitude and mobility similar to the ancestral sector collapse would directly affect over 11,000 people. This estimate does not include areas potentially affected by ash fall, ballistics, or an associated blast; a blast deposit from the ancestral sector collapse was mapped several kilometers outside of the debris avalanche deposits to the north and west of the cone (Fig. 5b; Kitamura and Matías, 1995).

#### 5.1.2. Investigating slope instability with space and air-borne InSAR

Both the co-eruptive linear collapse and the large lava flow that erupted during the 27–28 May 2010 eruption prompted concerns over the stability of the edifice (Matías Gómez et al., 2012). This led to an investigation into deformation surrounding the eruption using SAR data



from the Advanced Land Observing Satellite (ALOS-1, L-band where  $\lambda = 23.6$  cm) and aerial Uninhabited Aerial Vehicle Synthetic Aperture Radar (UAVSAR, L-band where  $\lambda = 23.8$  cm; UAVSAR data courtesy of NASA/JPL-Caltech).

Fig. 6 shows a time series of radar interferometry (PSI and InSAR) prior to, during, and after the explosive May 2010 eruption through to another period of heightened activity in January and March of 2014. PSI shows no evidence of continuous or episodic movement of the lower flank in the years (August 2007–March 2010) leading up to the 2010 eruption that would indicate long-term instability (Fig. 6b; Schaefer et al., 2017). Interferograms that span the May eruption contain dense fringes that form a semicircle from the Cerro Chino cone to the flank vents outside of the collapse scarp (Fig. 6c). Combining the different angles of UAVSAR and ALOS interferograms (see Schaefer et al., 2015a) and calculations of along-slope displacements (i.e. Zhao et al., 2012), the SW flank experienced  $\sim 270$  cm of westward and downslope motion. Notably, the deformation extends over the ancestral collapse scarp onto the older part of the edifice and abruptly stops in the plane of the 2010 lava flow (Fig. 6C). This is evidence that a NNW-trending magma intrusion produced the explosive eruption and likely initiated the SW slope movement (with the edge of the movement correlating with the edge of the intrusion), which ultimately drained out to produce the 2010 lava flow (discussed further in Section 5.1.4). Coherence, or signal correlation, breaks down at elevations above 1500 asl on the southwest

flank and 1700 asl on the west flank (pixilated regions in Fig. 6c), likely due to high deformation rates above InSAR detection limits within one 7.5 m pixel (11.8 cm in the case of ALOS), or changes of scattering properties within pixels due to thick ( $\sim 20$  cm) tephra deposition during the eruption.

Following the May eruption and slope movement, Pacaya went through a period of quiescence until late 2012. Interferograms show that the material on the SW flank resettled for several months after the landslide, until only small displacements near the summit area are measured in early 2011 (Fig. 6d–g; Schaefer et al., 2016). Cooling and subsidence of the 2010 lava flow is also evident during this time frame, which continues through 2015 (Wnuk and Wauthier, 2017). From December 2012 through December 2013, Pacaya was consistently degassing or producing small eruptions (generally confined to the summit vent, which produced varying cm-scale displacements on the upper cone (Wnuk and Wauthier, 2017), including an elongated NW-SE subsidence at the summit (Fig. 6h). Activity then increased in early January 2014 when it entered a major mixed effusive-explosive eruption phase from the 9–12 January 2014, producing two lava flows to the NW and SE of the summit vent (see Fig. 6a for outline of flows, and Fig. 6i for phase incoherence associated with flows). Interferograms during this time show a maximum of  $\sim 90$  cm of displacement (downward or westward) on the SW flank and  $\sim 19$  cm of opposite displacement (upward or eastward) on the E flank, characteristic of a “butterfly”

**Fig. 7.** Results of pixel offset measurements and conceptual model of flank movement. (A) Vertical and horizontal motion components from SAR amplitude pixel offset measurements. Arrows correspond to horizontal motion, with the length of the arrow corresponding to the displacement magnitude. Colored points correspond to vertical motion, with hotter colors indicating uplift and cooler colors indicating subsidence. GPS measurements (locations shown with black triangles) collected between 19 and 28 January 2009 and 20–26 January 2011 correlate well with InSAR measurements. Easting, northing, and vertical measurements in meters for each location are as follows: GPS 1,  $-0.0603$  (easting),  $-0.2561$  (northing), and  $-0.1965$  (vertical). GPS 2,  $-0.062$ , 0, and  $-0.022$ ; GPS 3,  $-0.104$ ,  $-0.216$ , and  $-0.161$ ; GPS 4,  $-0.023$ ,  $-0.025$ , and  $0.015$ . See Schaefer et al. (2017) for more details. (B) SW-NE model of the 2010 and ancestral slip surfaces based on field observations and satellite geodesy. The 2010 slip surface is drawn by extending the angle of surface movement inward, represented by dashed red lines, and the potential zone of unstable material is represented by the pink dashes. Figure modified from Schaefer et al. (2017). (For interpretation of the references to color in this figure legend, the reader is referred to the web version of this article.)

deformation pattern due to a dike intrusion (e.g. González et al., 2015). However, modeling of a dike intrusion cannot account for the full extent of asymmetric deformation on the western flank, and is thus partially attributed to co-eruptive slipping of the SW flank (descending and ascending UAVSAR interferograms shown in Fig. 6H&I; Wnuk and Wauthier, 2017).

### 5.1.3. Resolving 3D slope movement with SAR amplitude pixel offset measurements

To resolve 3D surface displacements, a pixel offset technique was applied to two pairs of coregistered UAVSAR SAR amplitude images acquired on 11 February 2010 and 26 April 2011 to determine unambiguous ground displacement measurements in both the LOS direction and parallel to the along-track satellite flying direction (Michel et al., 1999; Fialko et al., 2001). Cross-correlation windows were distributed throughout the amplitude images to detect strong reflectors, and azimuth and range offsets were estimated by cross correlating windows centered on the assigned locations. The 3-D displacement field was then calculated using a system of linear equations linking the azimuth and range offset measurements (see Schaefer et al., 2017 for methodology details). These measurements confirm high-magnitude landsliding movement of the SW flank, with the greatest amount of displacement occurring at higher elevations (maximum westward movement of  $3.92 \pm 0.02$  m, southward movement of  $2.90 \pm 0.04$  m, and downward movement of  $2.95 \pm 0.05$  m), decreasing in magnitude to the toe of the slide (Schaefer et al., 2017; Fig. 7a). It should be noted that although pixel offset tracking cannot recover deformation on the upper southwest flanks due to severe surface disturbances, based on the smooth deformation field and the spatial extent of settlement post-eruption (Schaefer et al., 2016), displacements are speculated to increase towards the summit, similar to the western flank. This is supported by significant deformation ( $\sim 20$  cm) of the ancestral collapse scarp located to the NNW of the linear collapse measured with GPS in January of 2009 and 2011 (see GPS 1, Fig. 7). The magnitude and direction of movement on the lower flanks is additionally supported by GPS measurements (Fig. 7; Schaefer et al., 2017). Amplitude pixel offset tracking increased measurement recovery by 48%, or an area increase of  $\sim 1.29 \text{ km}^2$ , over classic InSAR techniques, confirming that parts of the upper edifice were involved in the slope movement.

### 5.1.4. Implications for stability at Pacaya Volcano

The key questions for assessing slope stability hazards at Pacaya are: what causes flank movement, what (if any) conditions would trigger a catastrophic collapse, and is a collapse possible to forecast? Both the lack of long-term deformation prior to the slope movement (Fig. 6b; Schaefer et al., 2017), and a lack of continued slope movement after the May 2010 eruption (Fig. 6d-h; Schaefer et al., 2016), indicates that the movement was triggered rapidly when magma intruded into the cone during the 2010 eruptions, and then ceased in the early stages of sliding. After this point, the flank was essentially static through several small effusive and explosive eruptions until another large dike intrusion and eruption occurred in 2014 (Schaefer et al., 2016; Wnuk and Wauthier, 2017). Thus, Pacaya's SW flank appears to be gravitationally stable, and only becomes destabilized during relatively large magma intrusions into the cone. The magmatic influence on the stability of the flank is supported by numerical modeling of flank stability (Schaefer et al., 2013).

The vents of erupted lava flows between 2010 and 2014 follow a NNW-SSE trend (Fig. 6), which is a notable change from a seemingly chaotic pattern of effusive lava flow eruptions since 1961 (Matías Gómez et al., 2012). This, along with geodetic modeling (Wnuk and Wauthier, 2017), cracking along the NNW trend (Schaefer et al., 2016), and the orientation of the 2010 linear collapse, confirm a NNW to NW-trending tensional zone across the cone and orientation of preferential magma rise. The edge of the slope movement coinciding with the 2010 lava flow vent is additional evidence of the location and orientation of

the magma intrusion, which likely provided both the “push” to destabilize the slope during its explosive phase, and the source of the later effusive phase. Thus, since the 2010 eruption, a new stage of volcanic rifting seems to have initiated at Pacaya, which may be driving a positive feedback process where flank motion induced-extension drives rifting processes, or vice-versa. This is similar to surface magma plumbing system geometries seen at other volcanoes with previous sector collapses (e.g. Stromboli, Corazzato et al., 2008). On a larger scale, this orientation is likely controlled by the local transtensional (ENE-WSW  $\sigma_3$ -component) stress regime (Schaefer et al., 2013). If this process continues at Pacaya, repeated displacement events may lead to a reduction in strength along the shearing surface (e.g. Reid et al., 2010), increasing the probability of catastrophic collapse.

Large episodic movement surrounded by essentially static periods is often observed in non-volcanic environments (e.g. Petley et al., 2005). At volcanoes, this is often triggered by magma-induced flank displacement on the order of 10's of centimeters (e.g. Kilauea; Swanson et al., 1976). In these cases, intrusions seem to temporally increase pre-existing gravitational instabilities, even re-activating repeatedly (i.e. Delaney and Denlinger, 1999). It is important to note that the ALOS revisiting time of 46-days prevents the retrieval of deformation in the weeks, days, and hours leading up to the flank movement at Pacaya. Thus, the possibility of short-term deformation cannot be ruled out. RADARSAT interferograms in Wnuk and Wauthier (2017) show that all dike intrusions between December 2010 and March 2014 are preceded by deflation of magma reservoirs, and that non-explosive periods could be due to un-erupted magma that forms a seal and prevents magma degassing, leading to explosive eruptions.

Unlike the continuous movement often measured on unstable volcano flanks, evidence from persistent scatterer InSAR at Pacaya Volcano suggests that large flank movements or catastrophic collapse may not be detectable long before they occur. Instead, episodic movements initiated by magmatic intrusions or other rapid triggers may promote edifice instability. Without high-frequency geodetic monitoring during eruptive episodes, short-term indications of impending large movement may be missed, preventing timely warning. Although remote sensing techniques such as InSAR are capable of creating high density spatial maps of volcanic deformation, large movements can lead to decorrelation or unwrapping errors, prohibiting the extraction of useful measurements. Amplitude image pixel offset measurements applied to UAVSAR SAR images have proven capable of retrieving signal from decorrelated areas in SAR interferograms, allowing a 3-D displacement field to be estimated from the azimuth- and range-offset measurements. The resulting measurements provide insight into a unique landslide event at an active volcano with the potential to collapse catastrophically.

The good spatial coverage of the InSAR data have allowed the measurement of a very large slope movement that would have been undetected with GPS, seismic, or field observations alone, highlighting the utility of SAR for monitoring volcanic deformation and potential catastrophic slope instability. Remote monitoring is particularly useful at Pacaya, where nearly constant effusive and explosive activity makes it difficult to use ground-based techniques. The markedly improved quality of the UAVSAR interferograms over ALOS shows that there are several advantages to using zero-baseline and higher pixel-resolution SAR for resolving deformation details. Additionally, the uniqueness of this flank movement emphasizes the importance of differing SAR instrument look angles for resolving movement components.

## 5.2. Stromboli (Italy)

Stromboli is a volcanic island located in the Tyrrhenian Sea, off the northern coast of Sicily, Italy (Fig. 8). The volcano has experienced several large mass wasting phenomena, forming two depressions on its NW (Sciara del Fuoco; SdF) and SE flank, showing bilateral flank instability (Romagnoli et al., 2009). The volcano regrown within the SdF

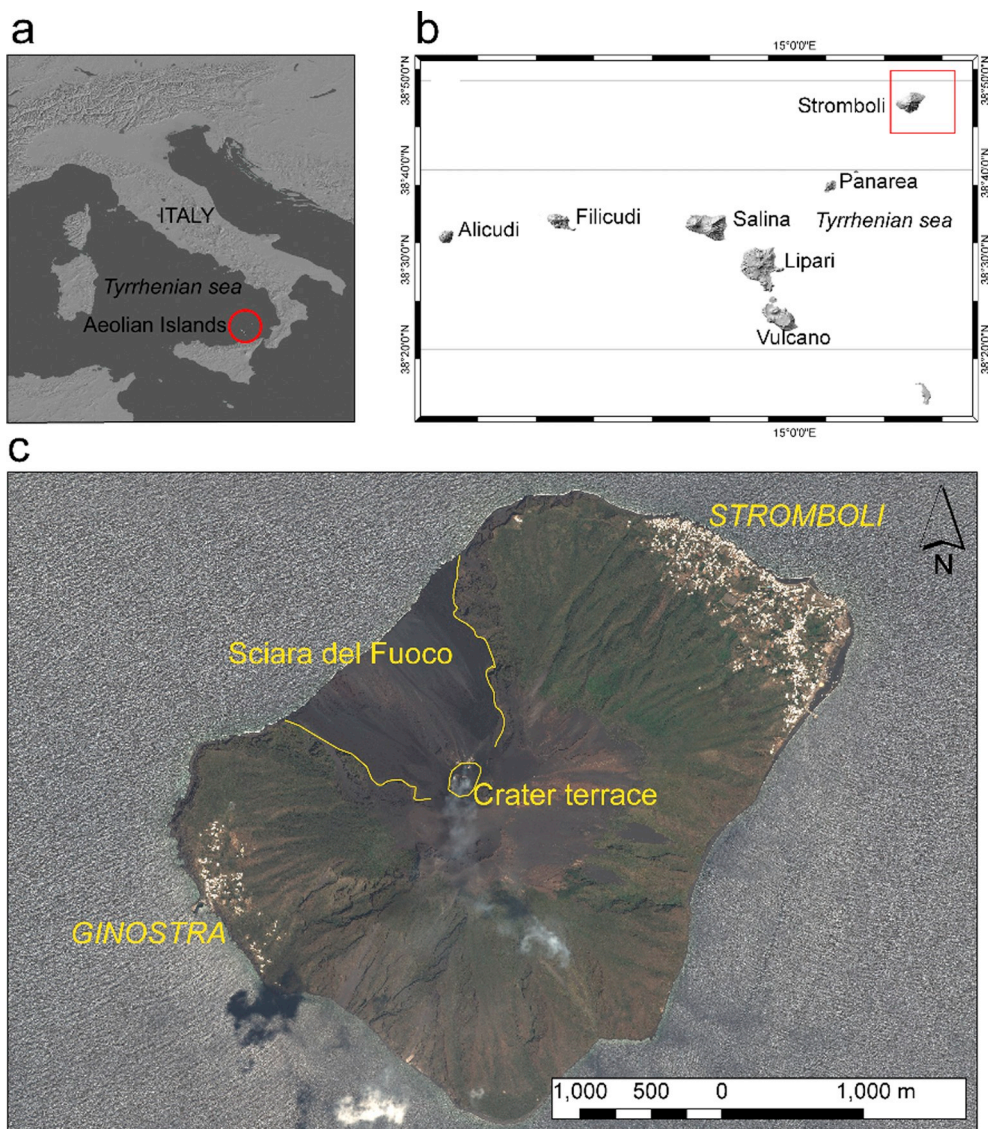


**Fig. 8.** Geographic location of (A) the Aeolian islands and (B) of the island of Stromboli. (C) PLEAIDES-1 orthorectified panchromatic image (true color, collected on August 2017) of the island of Stromboli. The locations of Stromboli and Ginostra villages, and the Sciara del Fuoco and the crater terrace are reported.

after the last large sector collapse occurred  $\approx 5.5$  ka (Tibaldi, 2001; Risica et al., 2018), and the depression is filled with volcaniclastic deposits and lavas (Rotonda et al., 2009; Nolesini et al., 2013), emitted from a summit crater terrace located at c. 750 m a.s.l., and from vents within the SdF (Calvari et al., 2005). The distinctive persistent Strombolian activity is characterized by intermittent explosions from three vent areas (NE, SW and Central) located in a summit crater terrace (Blackburn et al., 1976). This activity, showing intensity and frequency fluctuations over time, is often punctuated by lava overflows from the crater terrace (Taddeucci et al., 2013; Calvari et al., 2014), and/or by flank eruptions, with the outpouring of lava flows from lateral vents (Marsella et al., 2012).

#### 5.2.1. Slope instability and related hazards at Stromboli

At Stromboli, evidence of bi-lateral instability have been derived from geological observations in the sub-aerial and submarine part (e.g. Kokelaar and Romagnoli, 1995; Tibaldi, 2001; Tibaldi et al., 2009; Vezzoli and Corazzato, 2016). Present-day volcano slope instability comprises mobilization of coarse-grained and fine-grained sediments directly or indirectly related to the eruptive activity (Di Traglia et al., 2018c). During periods of low-intensity Strombolian activity, erosion is the prevailing process, whereas the production of materials ejected

from the crater terrace to the SdF is generally low. In contrast, sediment deposition in the SdF is the predominant phenomenon during periods of frequent or intense Strombolian activity or during flank eruptions, with the emplacement of grain flows and lava overflows (lava flows during flank eruptions; Di Traglia et al., 2018c). The planar deep creep of the SdF infill was proposed by Tibaldi et al. (2009) and measured (based on GBInSAR data) by Intrieri et al. (2013). The creep behavior has been related to both the presence of strata dipping parallel to the SdF slope and the infilling material having different rheological characteristics (volcaniclastic vs lava; Ter-Stepanian, 1966). Slope failures will produce a wide spectrum of mass movement phenomena, from small rockfalls (continuously affecting the SdF) to (debris) rotational or (rock) planar slides, evolving in (rock/debris) avalanches (Di Traglia et al., 2018c), and eventually triggering tsunamis (Tinti et al., 2006b; Nave et al., 2010). The most recent landslide of notable importance occurred soon after the onset of the 2002–03 flank eruption (Bonaccorso et al., 2003). The landslide was caused by the injection of a lateral intrusion (Neri et al., 2008) and observations indicated that a relatively deep seated scar ( $\approx 200$  m) affected the northern side of the Sciara del Fuoco (Baldi et al., 2008). The total submarine-sabreial landslide sequence removed a total volume of  $25\text{--}30 \times 10^6 \text{ m}^3$  (Chiocci et al., 2008) and generating two tsunamis, which affected the coastline with a maximum

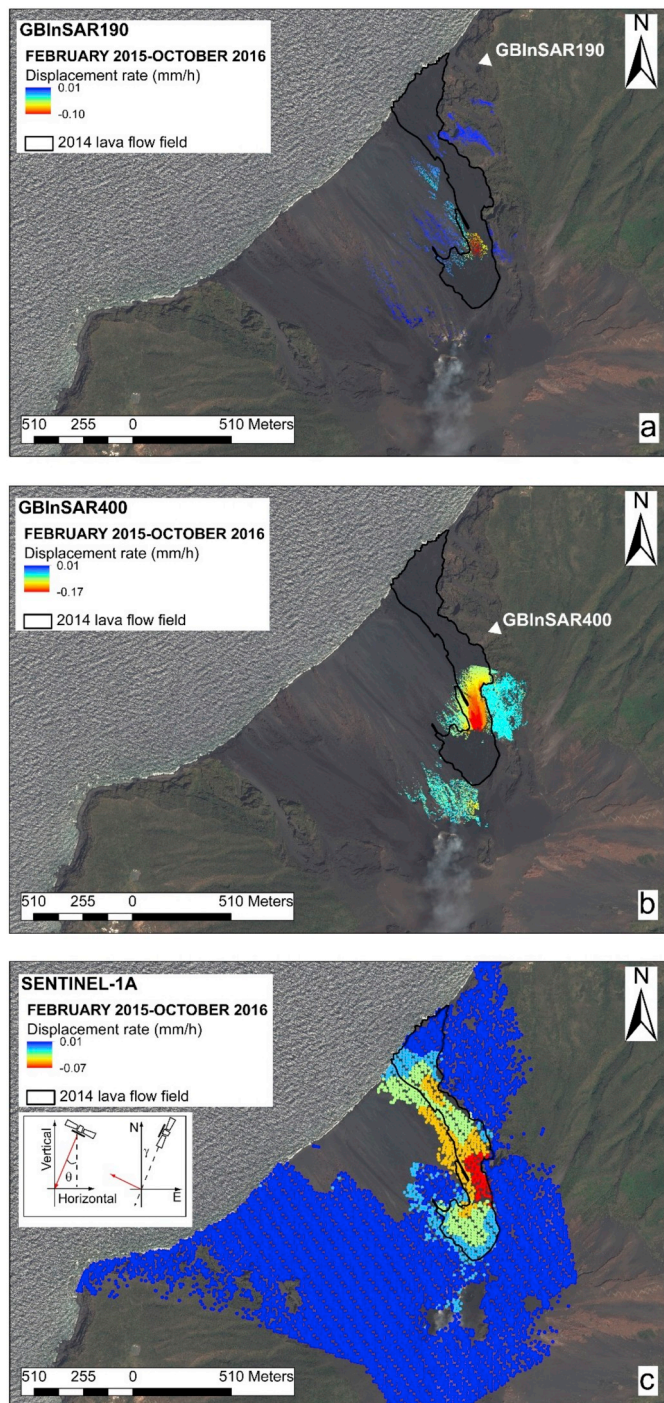


**Fig. 9.** Displacement maps for February 2015 – October 2016 based on the (A) GBInSAR NE190, (B) GBInSAR NE400, and (C) SENTINEL-1A data.

run-up of 6–7 m at the Stromboli village (Tinti et al., 2006a). Tsunamis also occurred in recent times as in 1879, 1916, 1919, 1930, 1944 and 1954, accounting for an average of 1 tsunami every 20 years (Maramai et al., 2005).

#### 5.2.2. Space and ground-based InSAR at Stromboli

The NE portion of the summit crater terrace and the northern portion of the SdF are monitored by two GBInSAR devices, located in a stable area N of the SdF (Fig. 9). The first GBInSAR (GBInSAR NE400; Model: GB-InSAR LiSALab; Revisiting time; 11 min; Antonello et al., 2004) was installed in February 2003, during the 2002–03 flank

eruption, while the second device (GBInSAR NE190; Model: GB-InSAR LiSAMobile k09; Revisiting time; 2 min) was installed on 14 December 2014, after the 2014 flank eruption. Moreover, a total of 47 SAR images from the C-band (5.6 GHz) SENTINEL-1A (SNT) satellite (23 February 2015–15 October 2016), in descending orbit, were exploited and processed using the SqueeSAR algorithm (Ferretti et al., 2011). To reduce the atmospheric disturbance Atmospheric Phase Screen (APS) filtering was performed (Ferretti et al., 2001; Di Traglia et al., 2018d).

#### 5.2.3. Surficial slope motion, co-eruptive displacement and mass wasting at Stromboli

The last flank eruption at Stromboli occurred between 7 August 2014 and 13 November 2014, and was preceded by 2 months of increased Strombolian activity, several lava overflows from the craters, and frequent landslides (rock falls and/or gravel/debris slides, evolving along the SdF to dry gravel/debris flows). The eruption was characterized by lava effusion in the SdF from a fracture 650 m above sea level, producing a lava flow field on the northern part of the SdF (Rizzo et al., 2015; Zálesk et al., 2015; Di Traglia et al., 2018a; Di Traglia et al., 2018d). The onset included several landslides that occurred in the afternoon of 6 August 2014, which involved the rim of the crater terrace and sliding of the debris talus located beneath the North East Crater (NEC; Fig. 10a). These landslides were concurrent with the opening of the eruptive vent on the morning of 7 August 2014 (Fig. 10b). At the time of the eruption, only the GBInSAR NE400 was installed and, in the period before the eruption (2010–2014), the crater terrace of Stromboli was characterized by movements towards and away from the sensor, consistent with either inflation or deflation of a deformation source located beneath the crater terrace, at a depth of  $482 \pm 46$  m a.s.l. (Di Traglia et al., 2015). The GBInSAR NE400 apparatus recorded the inflation of the summit plumbing system 2 months before the onset of the 2014 flank eruption (Di Traglia et al., 2015; Carlà et al., 2016a; Di Traglia et al., 2018b). Since 30 May 2014, the GBInSAR NE400 recorded a fluctuating displacement rate, however it was always above the threshold that distinguishes deformation from anomalous activity ( $> 0.05$  mm/h; see Di Traglia et al., 2014c for thresholds). Moreover, it measured an increase in the displacement rate (up to 230 mm/h, greatly exceeding the threshold that characterizes the “very high” activity;  $> 10$  mm/h) associated with the breaching of the summit area starting approximately 15 h before the occurrence of the collapse (Fig. 10c).

After the eruption, there were recorded displacements in the SdF related to three types of movement: (1) gravitational re-adjustment of the lava breccia, sometimes evolving in rockfalls (Di Traglia et al., 2018c), (2) thermal contraction of the lava field (Di Traglia et al., 2018d), and (3) persistent flank motion, particularly evident in the lava delta (i.e. a shelf of new land extending from the coastline produced by lava entering in the sea; see Poland and Orr, 2014; Fig. 9), and it is mechanically connected to the area of greatest submarine slope instability (Di Traglia et al., 2018a).

While the movements in the SdF were high after the eruption of 2014, the crater area showed very low displacement rates until December 2017, when the summit area started to inflate and spattering and overflows occurred. The activity was mainly located in the NEC area (Fig. 10), which led to the growth of the NEC cone outside the crater terrace, inside the 7 August 2014 landslide detachment area (Fig. 10b). High displacement rates were recorded in the NEC area by both GBInSAR devices. Two periods saw increases in the displacement rate above the thresholds defined by Di Traglia et al. (2014c). The first occurred on 15 December 2017, when a lava overflow occurred and the displacement rate increased (up to 22 mm/h), exceeding the threshold that characterizes the “very high” activity, ( $> 10$  mm/h). The other anomaly occurred between 17 and 18 December 2017, when several peaks of “very high” displacement rate (up to 130 mm/h) lasting 10 to 30 min occurred (Fig. 10d). These anomalies, despite their very high speeds, had fundamental differences with those recorded immediately

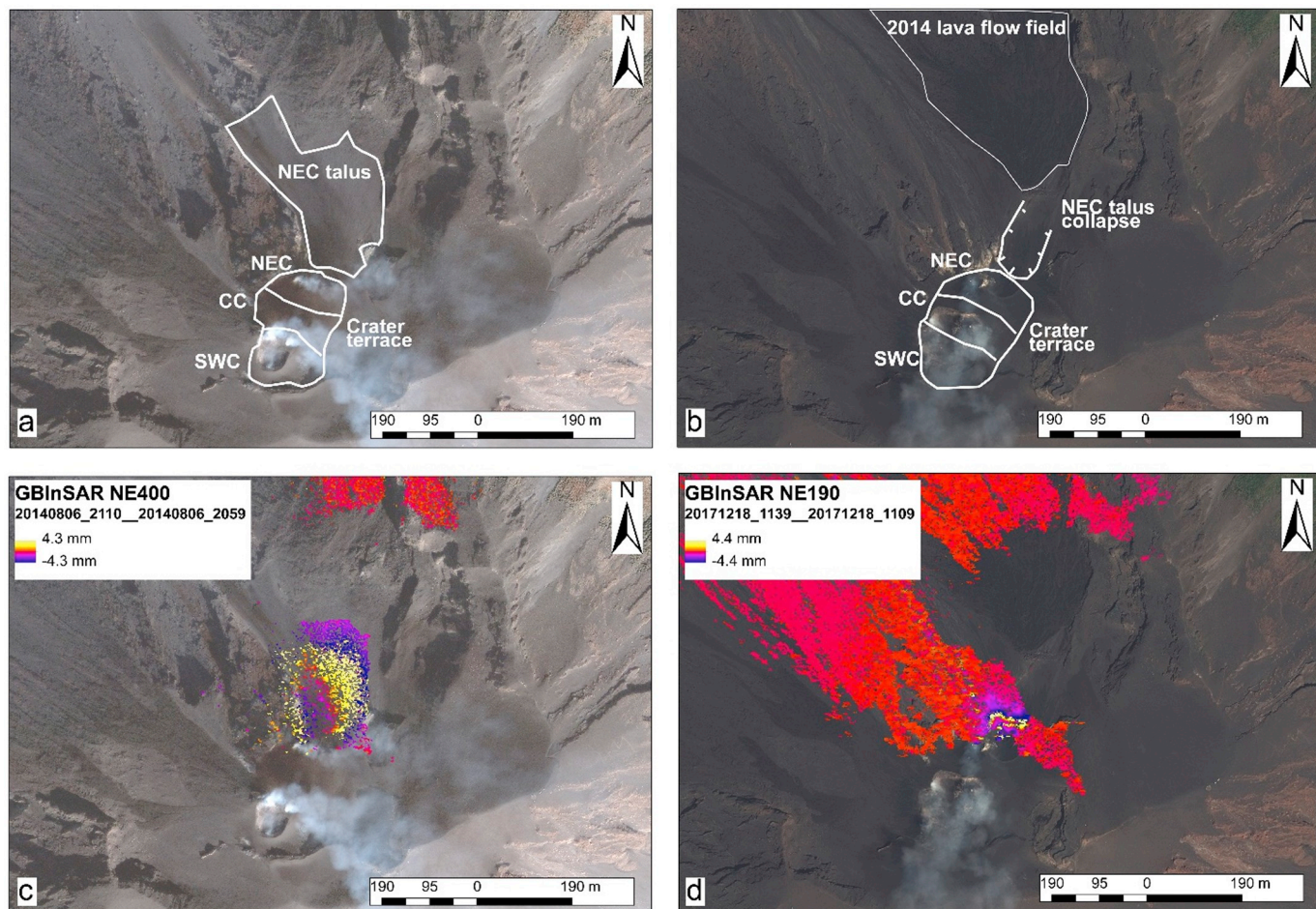


**Fig. 10.** The crater terrace and the upper part of the Sciara del Fuoco (A) before (true color, orthorectified, panchromatic QUICKBIRD image, collected on September 2012) and (B) after (true color, orthorectified, panchromatic PLEIADES-1 image, collected on August 2017) the 2014 flank eruption. The crater terrace, the NEC talus, and its collapse scarp formed on the 7 August 2014 are highlighted. Displacement related to the instability of the NEC talus as response of (C) fracture propagation before the onset of the 2014 flank eruption, and (D) during the spattering activity in December 2017.

before the start of the eruptions of 2007 and 2014: (a) they involved a small volume of material, which suggests that the collapse of the talus below the NEC, generally related to the magma migration process from the shallow reservoir to an lateral vent, was not occurring, and; (b) the destabilization of the NEC talus before the onsets of the 2007 and 2014 eruptions occurred as continuous and progressive phenomena (Casagli et al., 2009; Carlà et al., 2017). In this case, the destabilization events were impulsive, likely related to the instability of the NEC material emplaced during the spattering activity. Similar events were recorded during other periods of high volcanic activity (Calvari et al., 2016).

#### 5.2.4. Modeling lava contraction due to cooling at Stromboli

The contribution of lava cooling processes to overall deformation can be estimated through forward modeling if the thickness of the deposits is known (Chaussard, 2016). The deformation (subsidence) predicted by a cooling model can then be compared to the observed deformation to isolate the remaining contribution of slope instability.

A numerical 1-D model of lava cooling was developed for 2014 Stromboli flank eruption following the model of Chaussard (2016). Four vertical layers were included: the atmosphere maintained at 0 °C, the lava field with a starting temperature of 1230 °C (Zakšek et al., 2015) (with variable thicknesses based on the comparison between two DEMs collected before (May 2012) and after (May 2017) the eruption), the host rock receiving heat, and the host rock remaining at constant ambient temperature (deeper, 0 °C). Radiation and convection are considered at the interface between the atmosphere and the lava and

heat transfer within the flow and from the flow to the host rock is modeled using conduction (Chaussard, 2016). Density, emissivity, thermal conduction, specific heat capacity, latent heat of crystallization, crystal fraction, and porosity values are taken from Harris et al. (2005) and Apuani et al. (2005). Subsidence due to cooling is implemented following Biot (1956),

$$\Delta h(t) = h\eta [(1+\nu)/(1-\nu)]\Delta T(t) \quad (4)$$

where  $\eta$  is the coefficient of thermoelastic expansion taken as  $3.4 \cdot 10^{-5} \text{ }^{\circ}\text{C}^{-1}$ ,  $\nu$  is the Poisson's ratio of 0.25, and the temperature change,

$$\Delta T(h,t) = T_m - T_{av}(t) \quad (5)$$

with  $T_m$  the melt temperature (1230 °C) and  $T_{av}$  the average temperature of the flow. The cooling-induced subsidence rates were predicted for the period of SENTINEL-1 observations (2015–2016, Fig. 9), 2.2 years after emplacement.

Fig. 11c shows the 2015–2016 predicted cooling-induced subsidence rates. The maximum cooling-induced subsidence rate is ~80 mm/yr in the thickest part of the flow (35 m). The mean InSAR LOS velocity map (Fig. 11a) can be approximated as vertical deformation by considering the incidence angle of the satellite (vertical = LOSx1.22) to enable direct comparison of the predicted cooling-induced subsidence (Fig. 11c) with the observed deformation (Fig. 11a). While the cooling-induced subsidence is directly correlated with the lava thickness (Fig. 11b), the area with the maximum observed

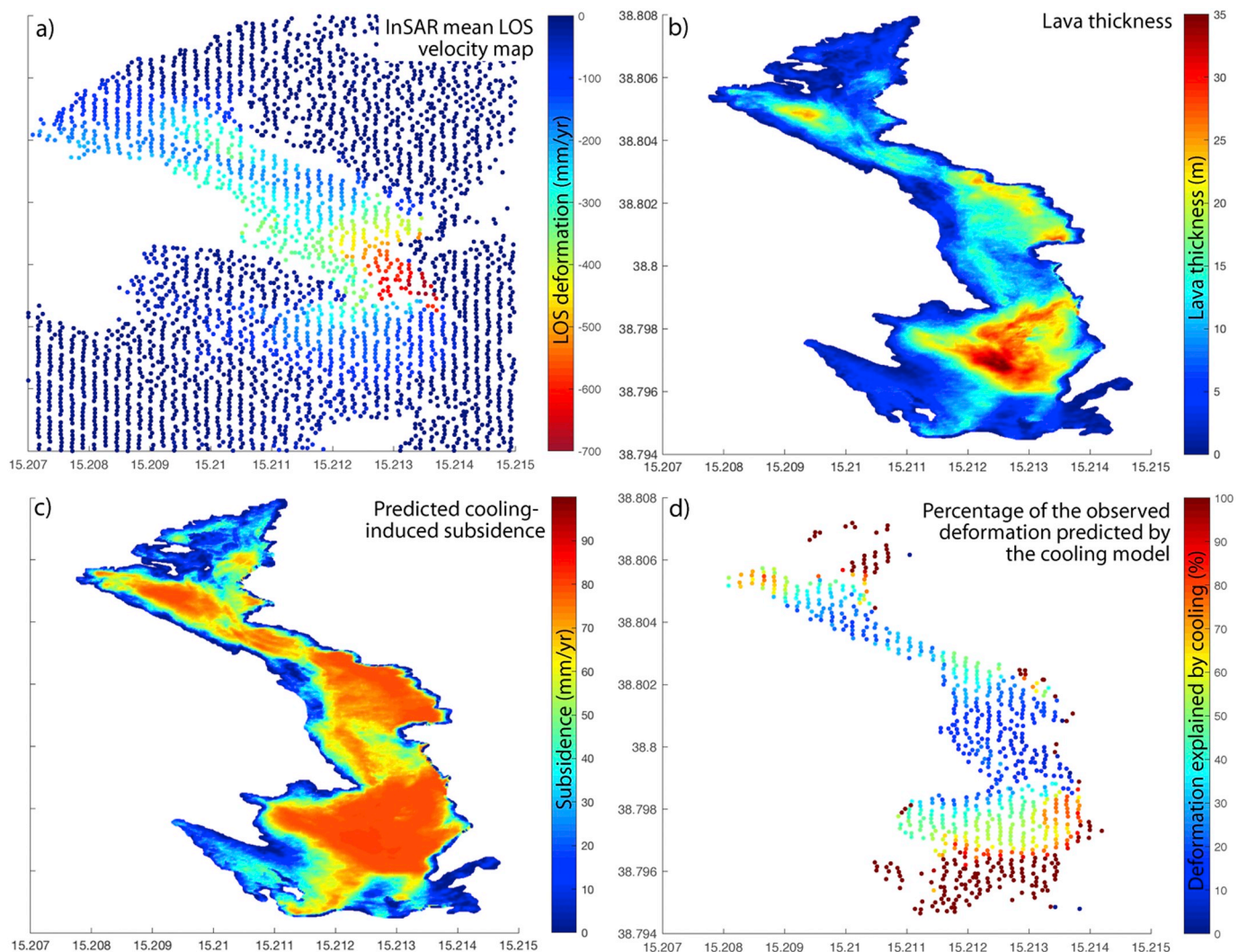


**Fig. 11.** (a) Observed 2015–2016 InSAR mean LOS velocity map; (b) Lava thickness based on the comparison between two DEMs collected before (May 2012) and after (May 2017) the eruption; (c) Cooling-induced subsidence predicted by the model. (d) Percentage of the observed deformation predicted by the contraction due to cooling model. While the cooling-induced subsidence (c) is directly correlated with the lava thickness (b), the area with the maximum observed displacement (a) is not.

displacement ( $\sim 700$  mm/yr) is in a flow only 10 m thick (Fig. 11a and b). For a 10 m thick flow, the cooling-induced subsidence predicted by the model is 60 mm/yr, which accounts for only  $\sim 9\%$  of the observed deformation ( $\sim 700$  mm/yr). In contrast, the predicted 80 mm/yr cooling-induced subsidence rate close to the summit corresponds to 72% of the observed deformation (110 mm/yr in a 35 m thick flow).

These results suggest that cooling-induced deformation accounts for only a limited part of the rapid flank motion observed during the 2014 Stromboli flank eruption (Fig. 11a and d). The area of maximum observed deformation (red in Fig. 11a) appears correlated with the slope angle rather than with the deposit thickness (red in Fig. 11b) and the associated cooling-induced deformation (red Fig. 11c). Slope instability is thus a more likely cause of the rapid deformation observed than compaction cooling processes.

#### 5.2.5. Modeling slope instability at Stromboli

The stability of the subaerial SdF slope was investigated by means of a 3D Limit Equilibrium Method (LEM) using the Scoops3D software (Reid et al., 2000; Reid et al., 2001). Scoops3D evaluates slope stability using a 3D version of the Bishop's simplified method of limit-equilibrium analysis considering rotational, spherical landslide surfaces using the factor of safety (F) equation shown in Section 2. Scoops3D computes

the volume and area associated with each of these potential landslides, determining also the least-stable potential failure surface for the entire digital elevation model. The numerical code also includes the option to represent subsurface materials by full 3D distributions of: (i) material cohesion, angle of internal friction, and weight; (ii) earthquake or seismic loading effects in a pseudo-static analysis; (iii) pore-water pressure effects, either with pore-pressure ratios (relative to vertical stresses), a piezometric surface or a full 3D distribution of pressure heads, and; (iv) fully 3D variably saturated groundwater flow fields and the effects of unsaturated suction stresses.

The LEM analysis was constructed considering two layers of subsurface materials:

- 1) alternation of lava layers (ranging from 35 to 65%) and breccia layers (Lava-Breccia Unit of Apuani et al., 2005), which constitute most of the subaerial SdF slope, and;
- 2) alternation of loose and hardened volcaniclastic layers, which constitute the central portion of the subaerial SdF slope (Volcaniclastic deposits; Apuani et al., 2005; Nolesini et al., 2013; Di Traglia et al., 2018d).

The geological model has been created starting from the comparison

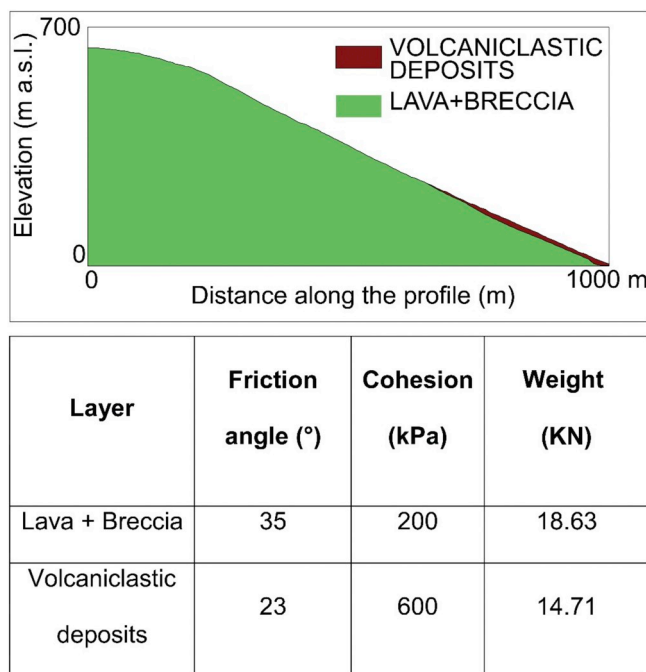


**Fig. 12.** Model set-up and material parameters. The Limit Equilibrium analysis has been made using Scoops3D software (Reid et al., 2015), considering two sub-surface material, accounting for the different distribution of lavas and volcaniclastic deposits. Following Lodato et al. (2007) and Di Traglia et al. (2018a), the recent lava flows were considered as alternation of lava layers (ranging from 35 to 65%) and breccia layers (Apuani et al., 2005), whereas the volcaniclastic deposits are considered prevailing pyroclastic breccias alternating with tuff and lapillistones (Apuani et al., 2005; Nolesini et al., 2013).

between two DEMs, collected before (May 2012) and after (May 2017) the 2014 flank eruption (Fig. 12). With the aim of modeling only the effect of the stability of the SdF slope, the lateral SdF edges have not been considered. The water table was assumed flat and coincident with sea level, representing the vertically hydrostatic pressure heads beneath the surface (water load on the slope). The pore pressure acting on the slope is defined by the vertical depth beneath the piezometric surface multiplied by the unit weight of water (Reid et al., 2015).

The pore pressure,  $u$ , is related to pressure head,  $h$  (in units of length) and water unit weight ( $\gamma_w$ ), by:

$$u = h\gamma_w \quad (6)$$

The unit weight ( $\gamma_s$ ), angle of internal friction and cohesion for dry SdF material (Apuani et al., 2005; Boldini et al., 2009; Nolesini et al., 2013) are used for the potential failure mass above the piezometric table. Material strength influence the size and location of the computed critical surfaces, and consequently also the type of landslide movement that may arise. This can be seen using the non-dimensional ratio  $I_{cs}$ , an index of cohesive to frictional strength:

$$I_{cs} = \frac{c}{\gamma H \tan \phi} \quad (7)$$

where  $c$  is cohesion,  $\gamma$  is material unit weight,  $H$  is hillslope height, and

**Table 3**

Instability scenarios and the associated hazards based on the results of the slope stability analysis.

Scenario	Expected phenomena	Volume range	Hazard level
1	Rockfalls and gravel slides eventually evolving in gravel flows	$10^3\text{--}10^4$	Low
2	Rockfalls and gravel slides eventually evolving in gravel flows	$10^4\text{--}10^5$	Low
3	Planar or rotation rock slides eventually evolving in rock/debris avalanches	$10^5\text{--}10^6$	Moderate
4	Planar or rotation rock slides eventually evolving in rock/debris avalanches	$10^6\text{--}10^7$	High to very high

$\phi$  is angle of internal friction (Janbu, 1954). For dry, cohesionless materials ( $I_{cs} = 0$ ), the critical surface is always shallow with minimal volume. Therefore, purely frictional strength with no pore pressures will result in shallow, planar, critical surfaces and the least-stable areas will likely merely reflect steep areas in the topography or planar, dipping, subsurface layer (planar slide). The volcaniclastic deposits filling the central part of the SdF were considered to have an angle of internal friction  $\phi$  of  $\sim 23^\circ$  with some cohesion (600 kPa). The lava fields were considered to have an angle of internal friction  $\phi$  of  $\sim 35^\circ$  with lower cohesion (200 kPa). This is consistent with the observations made after the 30 December 2002 landslides sequence (Tommasi et al., 2005). The stability analysis was conducted using four different ranges of landslide volumes (Table 3), considering small ( $10^4\text{--}10^5 \text{ m}^3$ ) to large ( $10^7\text{--}10^8 \text{ m}^3$ ) subaerial slope failures. F values between 0.9 and 1.1 always characterized the subaerial slope between 650 m a.s.l. and the coastline for all simulations (Fig. 13).

The four volume intervals allowed us to identify the unstable areas associated with different phenomena. While the two smaller volume ranges can be considered representative of the gravel/debris slide (eventually in the same location of rockfalls detachment areas), the two largest ones represent the rock slides and debris avalanches. Larger phenomena were not considered due to the uncertainty in the distribution of materials at depth.

From the LEM analysis results, different instability scenarios and the related level of hazard can be estimated. In the estimation of the latter the ability to generate tsunami was also taken into consideration. For landslides in the volume range of  $10^5\text{--}10^6 \text{ m}^3$ , a moderate hazard level results from two considerations: i) this kind of landslides do not generate tsunamis, as observed by Chiocci et al. (2008) and Calvari et al. (2016), and ii) analogue modeling suggested that a subaerial landslide could trigger a sub-marine one (Nolesini et al., 2013).

Di Traglia et al. (2014c) pushed InSAR technology beyond its limits, proposing an operational approach for the GBInSAR data a tool for mitigating the risk connected with the Sciara del Fuoco dynamics and the increase in eruptive activity (Table 4). This approach defined displacement rate thresholds and activity scenarios, based on the revision of ten years of volcanic activity. The approach was applied during the 2014 flank eruption, allowing the anticipation of the beginning of the eruption 11 h in advance.

However, in the eruptive period, the “displacement rate thresholds” approach was not sufficient to characterize the phenomena in progress, given that very high displacement rates were recorded but these were attributable to the instability of the lava breccia.

For this reason, an approach proposed considering both the displacement rate thresholds (quantitative approach) and the comparison between the extension and the location of the areas characterized by anomalous displacement rates and the results of the SdF stability models (qualitative approach) is employed. This coupled quantitative-qualitative methods enables estimating the order of magnitude of the volumes involved (Table 5).

## 6. Discussion and conclusive remarks

SAR data has been proven an invaluable tool for identifying ground deformation associated with magmatic, hydrothermal, tectonic, or other volcanic processes (Pinel et al., 2014). One of the main impacts of

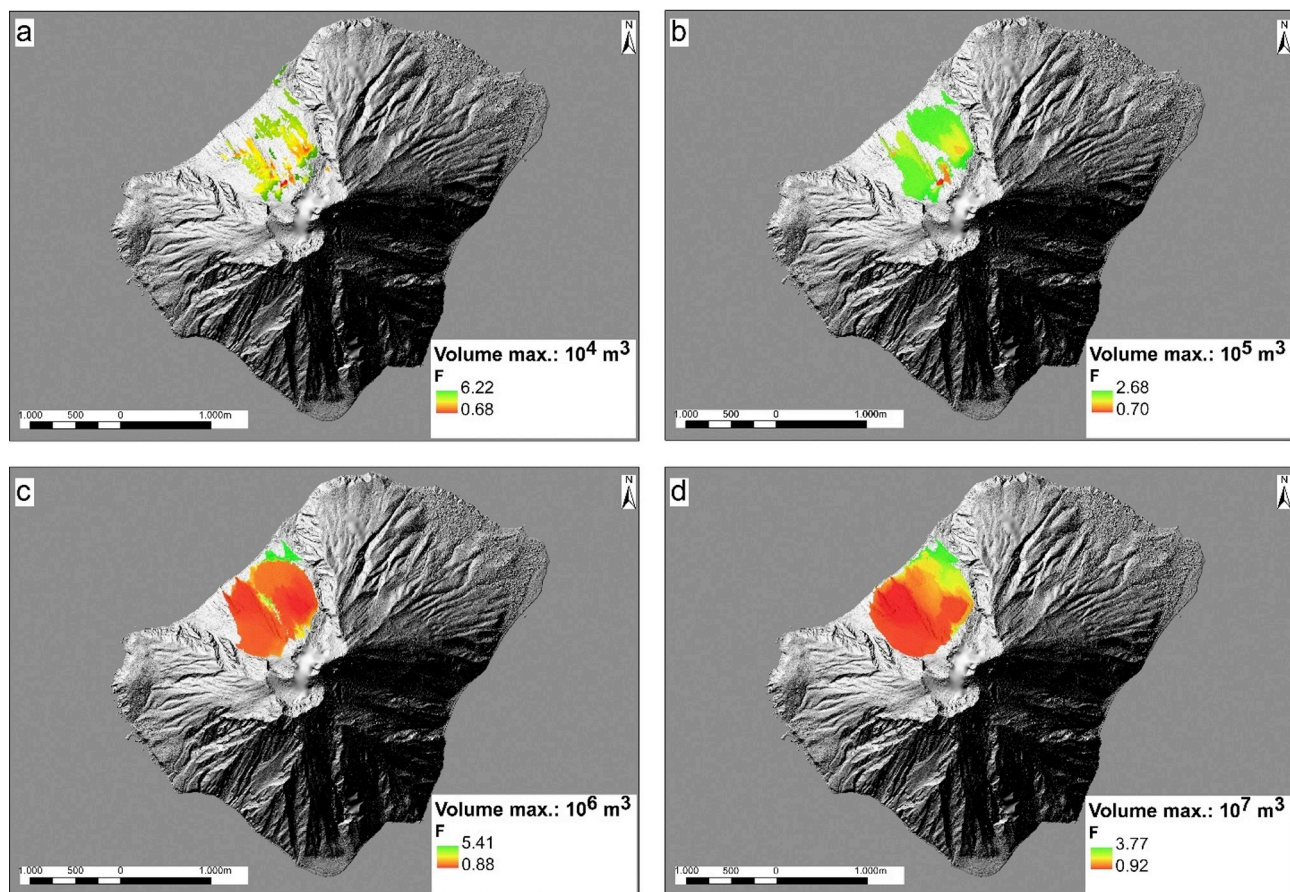


**Fig. 13.** Limit Equilibrium Analysis results for different landslide search volumes: (a) volumes ranging from  $10^3$  to  $10^4\text{ m}^3$ ; (b) volumes ranging from  $10^4$  to  $10^5\text{ m}^3$ ; (c) volumes ranging from  $10^5$  to  $10^6\text{ m}^3$ ; d) volumes ranging from  $10^6$  to  $10^7\text{ m}^3$ .

SAR studies have been used to detect unrest at volcanoes where no manifestations of activity had previously been reported (e.g. Pritchard and Simons, 2004), thereby improving risk assessments at volcanoes with otherwise limited data. Global SAR coverage has also greatly improved global databases with the goal for assessing, monitoring, and synthesizing volcanic deformation and associated hazards (e.g. Pritchard et al., 2018; Ebmeier et al., 2018). At the time of publication, over 485 deformation events have been detected at 221 volcanoes (Biggs and Pritchard, 2017), 160 of which were measured using SAR techniques.

This review has highlighted some of the key challenges for interpreting SAR data for the great variety of volcanic slope instability phenomena. We have provided several examples of different volcanic landslides of varying sizes and characteristics from around the world, and have attempted to combine measurements of current or recent volcano slope instability measured using SAR and other geodetic methods. These examples can be grouped into deep-seated persistent flank motion, deep-seated transient flank motion, and surficial flank

motion (persistent or transient), which all have different hazard implications and require observations from different SAR systems and processing techniques. An emphasis lies in the necessity of combining different methodologies, techniques, and analyses to discriminate the different phenomena that can occur simultaneously on a volcano flank/slope, as highlighted by both case studies of Pacaya and Stromboli volcanoes. In both of these cases, instability events have been successfully described or monitored by pairing SAR techniques with additional field, numerical, or geophysical studies. At Pacaya, while InSAR initially revealed a large transient landslide during an eruption in 2010, amplitude image pixel offset tracking techniques were required to improve measurement recovery and calculate the 3-D displacement field (Schaefer et al., 2017) which was supported by field GPS measurements (Schaefer et al., 2017). Evidence from structural studies and geotechnical and geodetic modeling additionally provided evidence to suggest that this event initiated a new stage of volcanic rifting at Pacaya, which has significant implications for slope stability

**Table 4**

Relationship between displacement rate in SdF and NEC talus (in brackets) and warning level, modified from Di Traglia et al. (2014c).

Displacement rate (mm/h)	Warning level	Expected instability phenomena	Expected eruptive phenomena
< 0.05	Low	Rockfalls and gravel slides eventually evolving in gravel flows	Strombolian activity
< 0.99 (< 9.99)	Moderate	Rockfalls and gravel slides eventually evolving in gravel flows	High intensity Strombolian activity
< 5 (< 50)	High	Planar or rotation rock slides eventually evolving in rock/debris avalanches	High intensity Strombolian activity / lava overflows
> 5 (> 50)	Very High	Planar or rotation rock slides eventually evolving in rock/debris avalanches	Lava flows

**Table 5**

Criticality level based on the intersection between the GBInSAR-derived warning levels (tidy) and the instability scenario based on the results of the slope stability analysis (abscissae).

Scenario (volume range)		1 ( $10^3$ – $10^4$ )	2 ( $10^4$ – $10^5$ )	2 ( $10^5$ – $10^6$ )	4 ( $10^6$ – $10^7$ )
Warning level		1 ( $10^3$ – $10^4$ )	2 ( $10^4$ – $10^5$ )	2 ( $10^5$ – $10^6$ )	4 ( $10^6$ – $10^7$ )
Low	Low	Low	Low	Low	Low
Moderate	Low		Moderate	Moderate	Moderate
High	Low		Moderate	High	High
Very high	Low		Moderate	High	Very high

(Schaefer et al., 2013; Schaefer et al., 2016; Wnuk and Wauthier, 2017).

Many studies have successfully interpreted complex deformation measured at volcanoes by pairing InSAR with other techniques. Muller et al. (2014) combined GPS, Total Station, and InSAR measurements to produce an integrated 3-D geodetic velocity surface of Arenal revealing a complex but constant ground deformation likely caused by the loading of lava on a layered basement. GBInSAR has been integrated with both geomorphological observations (Intrieri et al., 2013) and analog modeling (Nolesini et al., 2013) to understand the relationship between measured volcanic deformation, magma overpressure, and flank instability at Stromboli Volcano. Several studies also use geodetic modeling to refine interpretations of measured displacements or unravel complicated multi-process deformation patterns. For example, Lundgren et al. (2003) used a joint inversion of interferograms from both ascending and descending satellite tracks to successfully describe the simultaneous inflation of a magma chamber and slip of the east flank at Mt. Etna.

While SAR is now proven to be a useful tool for measuring volcanic landslides, most case histories measure deformation at volcanoes retroactively. At Stromboli, years of monitoring with ground-based InSAR (GBInSAR) resulted in an operational approach to mitigating landslide risks with SAR by defining a relationship between measured displacement rates and the associated instability and eruptive hazards (Di Traglia et al., 2014c). This aided in anticipating a flank eruption 11 h in advance in 2014, proving the potential of GBInSAR systems in early warning applications. Recently, the transition from static satellite analysis, used for mapping unstable areas, to dynamic monitoring of ground displacements was made possible through the use of the free-available, systematic and regular SAR observations SENTINEL-1 SAR data (e.g. Bianchini et al., 2018; Raspini et al., 2018; Solari et al., 2018). Monitoring landslides with radar has the potential to forecast landslide time of failures if displacements exhibit progressive acceleration (e.g. Intrieri et al., 2018), providing timely and high quality monitoring products. However, surveillance of mass wasting phenomena characterized by high displacement rates (surficial slope motion) or impulsive triggers (as dike intrusions responsible for transient flank motion) is possible only using ground-based sensors such GBInSAR devices. Studies of Stromboli have also highlighted the benefits of using numerical modeling to distinguish other volcanic processes from slope instability such as lava flow cooling and subsidence.

If persistent or steady state flank dynamics such as creep are detected at a volcano, determining what, if any, mitigatory actions is a significant challenge given the variety of persistent flank movement and the temporal and spatial variability of known events around the world. Slow moving non-volcanic landslide studies have benefited from rapid and updatable InSAR data acquisitions (e.g. Casagli et al., 2017), allowing for the detection and mapping of actively deforming slopes (e.g. Bianchini et al., 2014), as well as the characterization and monitoring of landslide mechanisms (e.g. Tofani et al., 2013). Based on long-term flank instability characteristics of several basaltic volcanoes, Poland et al. (2017) suggest a conceptual framework that positively

correlates a higher rate of flank motion with both increasing magma supply and greater thickness of the substrate, although exceptions do occur (e.g. surge in magma supply at Kilauea in 2003–2007 that caused no appreciable change in flank displacement rates; Poland et al., 2012; Poland, 2015; Anderson and Poland, 2016; Dzurisin et al., 2018).

The interoperability of SAR data can be greatly improved using numerical modeling. For example, models can be used to infer the basal plane geometry and slide thickness using the principle of mass conservation and 3D motion derived from descending and ascending SAR images (e.g. Hu et al., 2018). Unraveling different contributions to measured volcano deformation (separating multiple deformation signals) can also be improved from the use of statistical techniques such as principal component analysis, independent component analysis, cluster analysis (Ebmeier, 2016; Chaussard et al., 2017).

Monitoring slope instability over the world's volcanoes will be enhanced by the new radar satellites that are scheduled to launch around 2020–2021. These new sensors include L-band ALOS-4 PALSAR by JAXA (due to launch in 2020) (<http://global.jaxa.jp/projects/sat/ALOS4/>), L-band NISAR by NASA-India (due to launch in 2022) (<https://nisar.jpl.nasa.gov/>), L-band SAOCOM by Argentine Space Agency (due to launch in 2022–2023), and others. These L-band sensors will provide shorter repeats and much improved coherence and coverage than previous L-band sensors. Particularly, L-band NSAR will be operated in the left-looking mode. Combining descending and ascending InSAR images from both left-looking and right-looking modes will allow the construction of true 3D motion at an accuracy of centimeters. However, integrating satellite with in situ measurements is mandatory to account for proper 3D measurements, as well as for the operation use of deformation data in slope instability hazard management. If possible to install in safe areas, increasing the use of GBInSAR systems in monitoring networks can serve as potential surveillance tools where satellite data fails, as it provides frequent revisiting time, optimal viewing angles, and usable even in the presence of abundant ash in the atmosphere.

Looking ahead, there remains a need to make massive SAR datasets for the analysis of slope deformation interoperable. These big data pipelines can greatly benefit from cloud computing platforms (e.g. Zinno et al., 2018) that can fuse several datasets, including other types of geophysical data such as GPS. While these frameworks can improve the manageability and rapidity of large datasets, the sharing and usability of the output must also improve. Satellite data can provide actionable insight through means such as updated risk maps (i.e. ‘risk bulletins’; Raspini et al., 2018), operational mitigation tools for practitioners (i.e. Di Traglia et al., 2014c), or rapid-viewing platforms (e.g. <https://apps.sentinel-hub.com/ eo-browser/>; <https://worldview.earthdata.nasa.gov/>). With continued advancements in radar sensors and processing techniques, we can move beyond observing and explaining volcanic slope instability to forecasting and tracking failures, enhancing the mitigation of these potentially dangerous phenomena.

## Acknowledgments

This work was financially supported by the “Presidenza del Consiglio dei Ministri – Dipartimento della Protezione Civile” (Presidency of the Council of Ministers – Department of Civil Protection); this publication, however, does not reflect the position and official policies of the Department. SENTINEL-1A images were processed by TRE ALTAMIRA s.r.l. using the SqueeSAR technique. The authors are grateful to F. Bellotti, M. Luciani and A. Fumagalli (TRE ALTAMIRA s.r.l.) for technical support during the processing phase. This work was financially supported by the “Volcano Sentinel - extension” project (Call: “Settore ricerca scientifica e innovazione tecnologica”; funded by: Ente Cassa di Risparmio di Firenze. Scientific Responsibility: Federico Di Traglia).

## References

- Acocella, V., Puglisi, G., 2013. How to cope with volcano flank dynamics? A conceptual model behind possible scenarios for Mt. Etna. *J. Volcanol. Geotherm. Res.* 251, 137–148.
- Acocella, V., Behncke, B., Neri, M., D’Amico, S., 2003. Link between major flank slip and 2002–2003 eruption at Mt. Etna (Italy). *Geophys. Res. Lett.* 30 (24).
- Alloway, B., McComb, P., Neall, V., Vučetić, C., Gibb, J., Sherburn, S., Stirling, M., 2005. Stratigraphy, age, and correlation of voluminous debris-avalanche events from an ancestral Egmont Volcano: implications for coastal plain construction and regional hazard assessment. *J. R. Soc. N. Z.* 35 (1–2), 229–267.
- Amini, M., Majdi, A., Aydan, Ö., 2009. Stability analysis and the stabilisation of flexural toppling failure. *Rock Mech. Rock Eng.* 42 (5), 751–782.
- Anderson, K.R., Poland, M.P., 2016. Bayesian estimation of magma supply, storage, and eruption rates using a multiphysical volcano model: Kilauea Volcano, 2000–2012. *Earth Planet. Sci. Lett.* 447, 161–171.
- Antonello, G., Tarchi, D., Casagli, N., Farina, P., Guerri, L., Leva, D., 2004. SAR Interferometry from Satellite and Ground-Based System for Monitoring Deformations on the Stromboli Volcano, Geoscience and Remote Sensing Symposium, 2004. IGARSS’04. Proceedings. 2004, IEEE International (IEEE).
- Apuani, T., Corazzato, C., Cancelli, A., Tibaldi, A., 2005. Stability of a collapsing volcano (Stromboli, Italy): limit equilibrium analysis and numerical modelling. *J. Volcanol. Geotherm. Res.* 144 (1), 191–210.
- Baldi, P., Bosman, A., Chiocci, F.L., Marsella, M., Romagnoli, C., Sonnessa, A., 2008. Integrated subaerial-submarine morphological evolution of the Sciaro del Fuoco after the 2002 landslide. The Stromboli volcano: an integrated study of the 2002–2003 eruption. *AGU Geophys. Monogr.* Ser. 182, 171–182.
- Balme, M., Rocchi, V., Jones, C., Sammonds, P., Meredith, P., Boon, S., 2004. Fracture toughness measurements on igneous rocks using a high-pressure, high-temperature rock fracture mechanics cell. *J. Volcanol. Geotherm. Res.* 132 (2), 159–172.
- Begét, J.E., Kienle, J., 1992. Cyclic formation of debris avalanches at Mount St Augustine volcano. *Nature* 356 (6371), 701.
- Belousov, A., Voight, B., Belousova, M., 2007. Directed blasts and blast-generated pyroclastic density currents: a comparison of the Bezymianny 1956, Mount St Helens 1980, and Soufrière Hills, Montserrat 1997 eruptions and deposits. *Bull. Volcanol.* 69 (7), 701.
- Berardino, P., Fornaro, G., Lanari, R., Sansosti, E., 2002. A new algorithm for surface deformation monitoring based on small baseline differential SAR interferograms. *IEEE Trans. Geosci. Remote Sens.* 40 (11), 2375–2383.
- Bianchini, S., Tapete, D., Ciampalini, A., Di Traglia, F., Del Ventisette, C., Moretti, S., Casagli, N., 2014. Multi-temporal evaluation of landslide-induced movements and damage assessment in San Fratello (Italy) by means of C-and X-band PSI data. In: Mathematics of Planet Earth. Springer, pp. 257–261.
- Bianchini, S., Raspini, F., Solari, L., Del Soldato, M., Ciampalini, A., Rosi, A., Casagli, N., 2018. From picture to movie: twenty years of ground deformation recording over Tuscany Region (Italy) with satellite InSAR. *Front. Earth Sci.* 6, 177.
- Biggs, J., Pritchard, M.E., 2017. Global volcano monitoring: what does it mean when volcanoes deform? *Elements* 13 (1), 17–22.
- Biot, M.A., 1956. Thermoelasticity and irreversible thermodynamics. *J. Appl. Phys.* 27 (3), 240–253.
- Blackburn, E., Wilson, L., Sparks, R.S.J., 1976. Mechanisms and dynamics of strombolian activity. *J. Geol. Soc.* 132 (4), 429–440.
- Blahut, J., Klimeš, J., Rowberry, M., Kusák, M., 2018. Database of giant landslides on volcanic islands—first results from the Atlantic Ocean. *Landslides* 15 (4), 823–827.
- Boldini, D., Wang, F., Sassa, K., Tommasi, P., 2009. Application of large-scale ring shear tests to the analysis of tsunamigenic landslides at the Stromboli volcano, Italy. *Landslides* 6 (3), 231–240.
- Bonaccorso, A., Calvari, S., Garfi, G., Lodato, L., Patanè, D., 2003. Dynamics of the December 2002 flank failure and tsunami at Stromboli volcano inferred by volcanological and geophysical observations. *Geophys. Res. Lett.* 30 (18).
- Bonaccorso, A., Bonforte, A., Gambino, S., 2010. Thermal expansion-contraction and slope instability of a fumarole field inferred from geodetic measurements at Vulcano. *Bull. Volcanol.* 72 (7), 791–801.
- Bonforte, A., Guglielmino, F., 2015. Very shallow dyke intrusion and potential slope failure imaged by ground deformation: the 28 December 2014 eruption on Mount Etna. *Geophys. Res. Lett.* 42 (8), 2727–2733.
- Bonforte, A., Aloisi, M., Antonello, G., Casagli, N., Fortuny-Guash, J., Guerri, L., Nunnari, G., Puglisi, G., Spata, A. and Tarchi, D. (2008) Movements of the Sciaro del Fuoco, the Stromboli volcano: an integrated study of the 2002–2003 eruption: 183–199.
- Bonforte, A., Guglielmino, F., Coltellini, M., Ferretti, A., Puglisi, G., 2011. Structural assessment of Mount Etna volcano from Permanent Scatterers analysis. *Geochem. Geophys. Geosyst.* 12 (2).
- Borgia, A., de Vries, B.V.W., 2003. The volcano-tectonic evolution of Concepción, Nicaragua. *Bull. Volcanol.* 65 (4), 248.
- Borgia, A., Ferrari, L., Pasquare, G., 1992. Importance of gravitational spreading in the tectonic and volcanic evolution of Mount Etna. *Nature* 357 (6375), 231.
- Borgia, A., Tizzani, P., Solaro, G., Manzo, M., Casu, F., Luongo, G., Pepe, A., Berardino, P., Fornaro, G., Sansosti, E., 2005. Volcanic spreading of Vesuvius, a new paradigm for interpreting its volcanic activity. *Geophys. Res. Lett.* 32 (3).
- Calder, E., Luckett, R., Sparks, R., Voight, B., 2002. Mechanisms of lava dome instability and generation of rockfalls and pyroclastic flows at Soufrière Hills Volcano, Montserrat. *Geol. Soc. Lond. Mem.* 21 (1), 173–190.
- Calvari, S., Spampinato, L., Lodato, L., Harris, A.J., Patrick, M.R., Dehn, J., Burton, M.R., Andronico, D., 2005. Chronology and complex volcanic processes during the 2002–2003 flank eruption at Stromboli volcano (Italy) reconstructed from direct observations and surveys with a handheld thermal camera. *J. Geophys. Res. Solid Earth* 110 (B2).
- Calvari, S., Bonaccorso, A., Madonia, P., Neri, M., Liuzzo, M., Salerno, G., Behncke, B., Caltabiano, T., Cristaldi, A., Giuffrida, G., 2014. Major eruptive style changes induced by structural modifications of a shallow conduit system: the 2007–2012 Stromboli case. *Bull. Volcanol.* 76 (7), 841.
- Calvari, S., Intrieri, E., Di Traglia, F., Bonaccorso, A., Casagli, N., Cristaldi, A., 2016. Monitoring crater-wall collapse at active volcanoes: a study of the 12 January 2013 event at Stromboli. *Bull. Volcanol.* 78 (5), 39.
- Capra, L., 2006. Abrupt climatic changes as triggering mechanisms of massive volcanic collapses. *J. Volcanol. Geotherm. Res.* 155 (3–4), 329–333.
- Carlà, T., Intrieri, E., Di Traglia, F., Casagli, N., 2016a. A statistical-based approach for determining the intensity of unrest phases at Stromboli volcano (Southern Italy) using one-step-ahead forecasts of displacement time series. *Nat. Hazards* 84 (1), 669–683.
- Carlà, T., Raspini, F., Intrieri, E., Casagli, N., 2016b. A simple method to help determine landslide susceptibility from spaceborne InSAR data: the Montescaglioso case study. *Environ. Earth Sci.* 75 (24), 1492.
- Carlà, T., Intrieri, E., Di Traglia, F., Nolesini, T., Gigli, G., Casagli, N., 2017. Guidelines on the use of inverse velocity method as a tool for setting alarm thresholds and forecasting landslides and structure collapses. *Landslides* 14 (2), 517–534.
- Carracedo, J., 1994. The Canary Islands: an example of structural control on the growth of large oceanic-island volcanoes. *J. Volcanol. Geotherm. Res.* 60 (3–4), 225–241.
- Carracedo, J.C., Day, S.J., Guillou, H., Torrado, F.J.P., 1999. Giant quaternary landslides in the evolution of La Palma and El Hierro, Canary Islands. *J. Volcanol. Geotherm. Res.* 94 (1–4), 169–190.
- Carrasco-Núñez, G., Díaz-Castellón, R., Siebert, L., Hubbard, B., Sheridan, M.F., Rodríguez, S.R., 2006. Multiple edifice-collapse events in the Eastern Mexican Volcanic Belt: the role of sloping substrate and implications for hazard assessment. *J. Volcanol. Geotherm. Res.* 158 (1–2), 151–176.
- Carrasco-Núñez, G., Siebert, L. and Capra, L. (2011) Hazards from volcanic avalanches.
- Casagli, N., Tibaldi, A., Merri, A., Del Ventisette, C., Apuani, T., Guerri, L., Fortuny-Guash, J., Tarchi, D., 2009. Deformation of Stromboli Volcano (Italy) during the 2007 eruption revealed by radar interferometry, numerical modelling and structural geological field data. *J. Volcanol. Geotherm. Res.* 182 (3–4), 182–200.
- Casagli, N., Frodella, W., Morelli, S., Tofani, V., Ciampalini, A., Intrieri, E., Raspini, F., Rossi, G., Tanteri, L., Lu, P., 2017. Spaceborne, UAV and ground-based remote sensing techniques for landslide mapping, monitoring and early warning. *Geoenviro. Disasters* 4 (1), 9.
- Chaussard, E., 2016. Subsidence in the Parícutin lava field: causes and implications for interpretation of deformation fields at volcanoes. *J. Volcanol. Geotherm. Res.* 320, 1–11.
- Chaussard, E., Amelung, F., Aoki, Y., 2013a. Characterization of open and closed volcanic systems in Indonesia and Mexico using InSAR time series. *J. Geophys. Res. Solid Earth* 118 (8), 3957–3969.
- Chaussard, E., Amelung, F., Wdowinski, S., Cabral-Cano, E., 2013b. Magnitude and Extent of Land Subsidence in Central Mexico Revealed by Regional InSAR ALOS Time-Series Survey. (EGU General Assembly Conference Abstracts).
- Chaussard, E., Bürgmann, R., Fattah, H., Johnson, C., Nadeau, R., Taira, T., Johanson, I., 2015. Interseismic coupling and refined earthquake potential on the Hayward-Calaveras fault zone. *J. Geophys. Res. Solid Earth* 120 (12), 8570–8590.
- Chaussard, E., Milillo, P., Bürgmann, R., Perissin, D., Fielding, E.J., Baker, B., 2017. Remote sensing of ground deformation for monitoring groundwater management practices: application to the Santa Clara Valley during the 2012–2015 California drought. *J. Geophys. Res. Solid Earth* 122 (10), 8566–8582.
- Chen, K., Smith, J.D., Avouac, J.P., Liu, Z., Song, Y.T., Gualandi, A., 2019. Triggering of the Mw 7.2 Hawaii earthquake of May 4, 2018 by a dike intrusion. *Geophys. Res. Lett.* <https://doi.org/10.1029/2018GL081428>.
- Chiocci, F.L., Romagnoli, C., Tommasi, P., Bosman, A., 2008. The Stromboli 2002 tsunamigenic submarine slide: characteristics and possible failure mechanisms. *J. Geophys. Res. Solid Earth* 113 (B10).
- Ciampalini, A., Raspini, F., Bianchini, S., Frodella, W., Bardi, F., Lagomarsino, D., Di Traglia, F., Moretti, S., Proietti, C., Pagliari, P., 2015. Remote sensing as tool for development of landslide databases: the case of the Messina Province (Italy) geodatabase. *Geomorphology* 249, 103–118.
- Clarke, D., Brenguier, F., Frogner, J.-L., Shapiro, N., Peltier, A., Staudacher, T., 2013.

- Timing of a large volcanic flank movement at Piton de la Fournaise Volcano using noise-based seismic monitoring and ground deformation measurements. *Geophys. J. Int.* 195 (2), 1132–1140.
- Corazzato, C., Francalanci, L., Menna, M., Petrone, C., Renzulli, A., Tibaldi, A., Vezzoli, L., 2008. What controls sheet intrusion in volcanoes? Structure and petrology of the Stromboli sheet complex, Italy. *J. Volcanol. Geotherm. Res.* 173 (1), 26–54.
- Crosetto, M., Monserrat, O., Cuevas-González, M., Devanthery, N., Crippa, B., 2016. Persistent scatterer interferometry: a review. *ISPRS J. Photogramm. Remote Sens.* 115, 78–89.
- Day, S., 1996. Hydrothermal pore fluid pressure and the stability of porous, permeable volcanoes. *Geol. Soc. Lond. Spec. Publ.* 110 (1), 77–93.
- De Vries, B.V.W., Borgia, A., 1996. The role of basement in volcano deformation. *Geol. Soc. Lond. Spec. Publ.* 110 (1), 95–110.
- De Vries, B.V.W., Davies, T., 2015. Landslides, Debris Avalanches, and Volcanic Gravitational Deformation, the Encyclopedia of Volcanoes, 2nd ed. Elsevier, pp. 665–685.
- De Vries, B.V.W., Francis, P., 1997. Catastrophic collapse at stratovolcanoes induced by gradual volcano spreading. *Nature* 387 (6631), 387–390.
- Delaney, P.T., Denlinger, R.P., 1999. Stabilization of volcanic flanks by dike intrusion: an example from Kilauea. *Bull. Volcanol.* 61 (6), 356–362.
- Delaney, P.T., Denlinger, R.P., Lisowski, M., Miklius, A., Okubo, P.G., Okamura, A.T., Sako, M.K., 1998. Volcanic spreading at Kilauea, 1976–1996. *J. Geophys. Res. Solid Earth* 103 (B8), 18003–18023.
- Derrien, A., Villeneuve, N., Peltier, A., Beauducel, F., 2015. Retrieving 65 years of volcano summit deformation from multitemporal structure from motion: the case of Piton de la Fournaise (La Réunion Island). *Geophys. Res. Lett.* 42 (17), 6959–6966.
- Di Traglia, F., Del Ventisette, C., Rosi, M., Mugnai, F., Intrieri, E., Moretti, S., Casagli, N., 2013. Ground-based InSAR reveals conduit pressurization pulses at S tromboli volcano. *Terra Nova* 25 (3), 192–198.
- Di Traglia, F., Cauchie, L., Casagli, N., Saccorotti, G., 2014a. Decrypting geophysical signals at Stromboli Volcano (Italy): integration of seismic and ground-based InSAR displacement data. *Geophys. Res. Lett.* 41 (8), 2753–2761.
- Di Traglia, F., Intrieri, E., Nolesini, T., Bardi, F., Del Ventisette, C., Ferrigno, F., Frangioni, S., Frodella, W., Gigli, G., Lotti, A., 2014b. The ground-based InSAR monitoring system at Stromboli volcano: linking changes in displacement rate and intensity of persistent volcanic activity. *Bull. Volcanol.* 76 (2), 786.
- Di Traglia, F., Nolesini, T., Intrieri, E., Mugnai, F., Leva, D., Rosi, M., Casagli, N., 2014c. Review of ten years of volcano deformations recorded by the ground-based InSAR monitoring system at Stromboli volcano: a tool to mitigate volcano flank dynamics and intense volcanic activity. *Earth Sci. Rev.* 139, 317–335.
- Di Traglia, F., Battaglia, M., Nolesini, T., Lagomarsino, D., Casagli, N., 2015. Shifts in the eruptive styles at Stromboli in 2010–2014 revealed by ground-based InSAR data. *Sci. Rep.* 5, 13569.
- Di Traglia, F., Bartolini, S., Artesi, E., Nolesini, T., Ciampalini, A., Lagomarsino, D., Martí, J., Casagli, N., 2018a. Susceptibility of intrusion-related landslides at volcanic islands: the Stromboli case study. *Landslides* 15 (1), 21–29.
- Di Traglia, F., Calvari, S., D'Auria, L., Nolesini, T., Bonaccorso, A., Fornaciai, A., Esposito, A., Cristaldi, A., Favalli, M., Casagli, N., 2018b. The 2014 Effusive Eruption at Stromboli: new insights from in situ and remote-sensing measurements. *Remote Sens.* 10 (12), 2035.
- Di Traglia, F., Nolesini, T., Ciampalini, A., Solaro, L., Frodella, W., Bellotti, F., Fumagalli, A., De Rosa, G., Casagli, N., 2018c. Tracking morphological changes and slope instability using spaceborne and ground-based SAR data. *Geomorphology* 300, 95–112.
- Di Traglia, F., Nolesini, T., Solaro, L., Ciampalini, A., Frodella, W., Steri, D., Allotta, B., Rindi, A., Marini, L., Monni, N., 2018d. Lava delta deformation as a proxy for submarine slope instability. *Earth Planet. Sci. Lett.* 488, 46–58.
- Dumont, S., Sigmundsson, F., Parks, M.M., Drouin, V.J., Pedersen, G., Jónsdóttir, I., Höskuldsson, Á., Hooper, A., Spaans, K., Bagnardi, M., Gudmundsson, M.T., Barsotti, S., Jónsdóttir, K., Högnadóttir, T., Magnússon, E., Hjartardóttir, Á.R., Þuríg, T., Rossi, C., Oddsson, B., 2018. Integration of SAR data into monitoring of the 2014–2015 Holuhraun eruption, Iceland: contribution of the Icelandic Volcanoes Supersite and the FutureVolc projects. *Front. Earth Sci.* 6, 231.
- Dzurisin, D., Lu, Z., Poland, M.P., Wicks, C.W., 2018. Space-based imaging radar studies of US volcanoes—past, present, and future. *Front. Earth Sci.* 6, 249.
- Ebmeier, S., 2016. Application of independent component analysis to multitemporal InSAR data with volcanic case studies. *J. Geophys. Res. Solid Earth* 121 (12), 8970–8986.
- Ebmeier, S., Biggs, J., Mather, T., Wadge, G., Amelung, F., 2010. Steady downslope movement on the western flank of Arenal volcano, Costa Rica. *Geochem. Geophys. Geosyst.* 11 (12).
- Ebmeier, S.K., Biggs, J., Muller, C., Avard, G., 2014. Thin-skinned mass-wasting responsible for widespread deformation at Arenal volcano. *Front. Earth Sci.* 2, 35.
- Ebmeier, S., Andrews, B., Araya, M., Arnold, D., Biggs, J., Cooper, C., Cottrell, E., Furtney, M., Hickey, J., Jay, J., 2018. Synthesis of global satellite observations of magmatic and volcanic deformation: implications for volcano monitoring & the lateral extent of magmatic domains. *J. Appl. Volcanol.* 7 (1), 2.
- Eggers, A.A., 1971. The Geology and Petrology of the Amatitlán Quadrangle. Guatemala. Eggers, A.A., 1983. Temporal gravity and elevation changes at Pacaya volcano, Guatemala. *J. Volcanol. Geotherm. Res.* 19 (3), 223–237.
- Elliott, J., Walters, R., Wright, T., 2016. The role of space-based observation in understanding and responding to active tectonics and earthquakes. *Nat. Commun.* 7, 13844.
- Fernández, J., Tizzani, P., Manzo, M., Borgia, A., González, P., Martí, J., Pepe, A., Camacho, A., Casu, F., Berardino, P., 2009. Gravity-driven deformation of Tenerife measured by InSAR time series analysis. *Geophys. Res. Lett.* 36 (4).
- Ferretti, A., Prati, C., Rocca, F., 2001. Permanent scatterers in SAR interferometry. *IEEE Trans. Geosci. Remote Sens.* 39 (1), 8–20.
- Ferretti, A., Fumagalli, A., Novali, F., Prati, C., Rocca, F., Rucci, A., 2011. A new algorithm for processing interferometric data-stacks: SqueeSAR. *IEEE Trans. Geosci. Remote Sens.* 49 (9), 3460–3470.
- Fialko, Y., Simons, M., Agnew, D., 2001. The complete (3-D) surface displacement field in the epicentral area of the 1999 Mw7.1 Hector Mine earthquake, California, from space geodetic observations. *Geophys. Res. Lett.* 28 (16), 3063–3066.
- Francis, P., Wells, G., 1988. Landsat Thematic Mapper observations of debris avalanche deposits in the Central Andes. *Bull. Volcanol.* 50 (4), 258–278.
- Froger, J.-L., Fukushima, Y., Briole, P., Staudacher, T., Souriot, T., Villeneuve, N., 2004. The deformation field of the August 2003 eruption at Piton de la Fournaise, Reunion Island, mapped by ASAR interferometry. *Geophys. Res. Lett.* 31 (14).
- Froger, J.-L., Famin, V., Cayol, V., Augier, A., Michon, L., Lénat, J.-P., 2015. Time-dependent displacements during and after the April 2007 eruption of Piton de la Fournaise, revealed by interferometric data. *J. Volcanol. Geotherm. Res.* 296, 55–68.
- Garthwaite, M.C., Miller, V.L., Saunders, S., Parks, M.M., Hu, G., Parker, A.L., 2018. A simplified approach to operational InSAR monitoring of volcano deformation in low- and middle-income countries: case study of Rabaul Caldera, Papua New Guinea. *Front. Earth Sci.* 6, 240.
- Glicken, 1996. Rockslide-Debris Avalanche of May 18, 1980, Mount St. Helens volcano, Washington. 2331–1258. (US Geological Survey).
- González, P.J., Tiampo, K.F., Camacho, A.G., Fernández, J., 2010. Shallow flank deformation at Cumbre Vieja volcano (Canary Islands): implications on the stability of steep-sided volcano flanks at oceanic islands. *Earth Planet. Sci. Lett.* 297 (3–4), 545–557.
- González, P.J., Bagnardi, M., Hooper, A.J., Larsen, Y., Marinkovic, P., Samsonov, S.V., Wright, T.J., 2015. The 2014–2015 eruption of Fogo volcano: geodetic modeling of Sentinel-1 TOPS interferometry. *Geophys. Res. Lett.* 42 (21), 9239–9246.
- Goodman, R.E. and Bray, J.W. (1976) Toppling of rock slopes, Proc. Speciality Conference on Rock Engineering for Foundation and Slopes. ASCE, pp. 201–234.
- Gross, F., Krastel, S., Urlaub, M., Geersen, J., Behrmann, J., Papenberg, C., Bialas, J., Koch, S., Crutchley, G., Micallef, A., 2016. Coupled Volcano Edifice-and-Continental Margin Deformation and Instability at Mt Etna. (Italy).
- Guthrie, R., Friele, P., Allstadt, K., Roberts, N., Evans, S., Delaney, K., Roche, D., Clague, J., Jakob, M., 2012. The 6 August 2010 Mount Meager rock slide-debris flow, Coast Mountains, British Columbia: characteristics, dynamics, and implications for hazard and risk assessment. *Nat. Hazards Earth Syst. Sci.* 12 (5), 1277–1294.
- Gylfadóttir, S.S., Kim, J., Helgason, J.K., Brynjólfsson, S., Höskuldsson, Á., Jóhannesson, T., Harbitz, C.B., Lövholt, F., 2017. The 2014 Lake Askja rockslide-induced tsunami: optimization of numerical tsunami model using observed data. *J. Geophys. Res. Oceans* 122 (5), 4110–4122.
- Harris, A., Dehn, J., Patrick, M., Calvari, S., Ripepe, M., Lodato, L., 2005. Lava effusion rates from hand-held thermal infrared imagery: an example from the June 2003 effusive activity at Stromboli. *Bull. Volcanol.* 68 (2), 107–117.
- Heap, M.J., Kennedy, B.M., Pernin, N., Jacquemard, L., Baud, P., Farquharson, J.I., Scheu, B., Lavallée, Y., Gilg, H.A., Letham-Brake, M., 2015. Mechanical behaviour and failure modes in the Whakaari (White Island volcano) hydrothermal system, New Zealand. *J. Volcanol. Geotherm. Res.* 295, 26–42.
- Herd, R.A., Edmonds, M., Bass, V.A., 2005. Catastrophic lava dome failure at Soufrière Hills volcano, Montserrat, 12–13 July 2003. *J. Volcanol. Geotherm. Res.* 148 (3–4), 234–252.
- Hibert, C., Mangeney, A., Grandjean, G., Peltier, A., DiMuro, A., Shapiro, N.M., Ferrazzini, V., Boissier, P., Durand, V., Kowalski, P., 2017. Spatio-temporal evolution of rockfall activity from 2007 to 2011 at the Piton de la Fournaise volcano inferred from seismic data. *J. Volcanol. Geotherm. Res.* 333, 36–52.
- Hildenbrand, A., Marques, F., Catalão, J., Catita, C., Costa, A., 2012. Large-scale active slump of the southeastern flank of Pico Island, Azores. *Geology* 40 (10), 939–942.
- Hildenbrand, A., Marques, F.O., Catalão, J., 2018. Large-scale mass wasting on small volcanic islands revealed by the study of Flores Island (Azores). *Scientific reports* 8 (1), 13898.
- Hooper, A., 2008. A multi-temporal InSAR method incorporating both persistent scatterer and small baseline approaches. *Geophys. Res. Lett.* 35 (16).
- Hu, J., Li, Z., Ding, X., Zhu, J., Zhang, L., Sun, Q., 2014. Resolving three-dimensional surface displacements from InSAR measurements: a review. *Earth Sci. Rev.* 133, 1–17.
- Hu, X., Lu, Z., Pierson, T.C., Kramer, R., George, D.L., 2018. Combining InSAR and GPS to determine transient movement and thickness of a seasonally active low-gradient translational landslide. *Geophys. Res. Lett.* 45 (3), 1453–1462.
- Hungr, O., Leroueil, S., Picarelli, L., 2014. The Varnes classification of landslide types, an update. *Landslides* 11 (2), 167–194.
- Hunt, J.E., Jarvis, I., 2017. Prodigious submarine landslides during the inception and early growth of volcanic islands. *Nat. Commun.* 8 (1), 2061.
- Hunt, J.E., Cassidy, M., Talling, P.J., 2018. Multi-stage volcanic island flank collapses with coeval explosive caldera-forming eruptions. *Sci. Rep.* 8 (1), 1146.
- Intrieri, E., Di Traglia, F., Del Ventisette, C., Gigli, G., Mugnai, F., Luzi, G., Casagli, N., 2013. Flank instability of Stromboli volcano (Aeolian Islands, Southern Italy): integration of GB-InSAR and geomorphological observations. *Geomorphology* 201, 60–69.
- Intrieri, E., Raspini, F., Fumagalli, A., Lu, P., Del Conte, S., Farina, P., Allievi, J., Ferretti, A., Casagli, N., 2018. The Maoxian landslide as seen from space: detecting precursors of failure with Sentinel-1 data. *Landslides* 15 (1), 123–133.
- Janbu, N., 1954. Application of Composite Slip Surface for Stability Analysis. Proceedings of European Conference on Stability of Earth Slopes, Sweden, pp. 43–49.
- Johnson, R., 1987. Large-scale volcanic cone collapse: the 1888 slope failure of Ritter volcano, and other examples from Papua New Guinea. *Bull. Volcanol.* 49 (5), 669–679.

- Jung, H.-S., Lu, Z., Won, J.-S., Poland, M.P., Miklius, A., 2011. Mapping three-dimensional surface deformation by combining multiple-aperture interferometry and conventional interferometry: application to the June 2007 eruption of Kilauea volcano, Hawaii. *IEEE Geosci. Remote Sens. Lett.* 8 (1), 34–38.
- Keating, B.H., McGuire, W., 2000. Island edifice failures and associated tsunami hazards. *Pure Appl. Geophys.* 157 (6–8), 899–955.
- Kendrick, J.E., Smith, R., Sammonds, P., Meredith, P.G., Dainty, M., Pallister, J.S., 2013. The influence of thermal and cyclic stressing on the strength of rocks from Mount St. Helens, Washington. *Bull. Volcanol.* 75 (7), 1–12.
- Kennedy, B., Holohan, E., Stix, J., Gravley, D., Davidson, J., Cole, J., 2017. Magma plumbing beneath collapse caldera volcanic systems. *Earth Sci. Rev.* 177, 404–424.
- Kerle, N., 2002. Volume estimation of the 1998 flank collapse at Casita volcano, Nicaragua: a comparison of photogrammetric and conventional techniques. *Earth Surf. Process. Landf.* 27 (7), 759–772.
- Kitamura, S., Matias, O., 1995. Tephra stratigraphic approach to the eruptive history of Pacaya volcano, Guatemala. *Sci. Rep.–Tohoku Univ., Seventh Ser.: Geogr.* 45 (1), 1–41.
- Kokeloa, P., Romagnoli, C., 1995. Sector collapse, sedimentation and clast population evolution at an active island-arc volcano: Stromboli, Italy. *Bull. Volcanol.* 57 (4), 240–262.
- Kuraoka, S., Nakashima, Y., Doke, R., Mannen, K., 2018. Monitoring ground deformation of eruption center by ground-based interferometric synthetic aperture radar (GB-InSAR): a case study during the 2015 phreatic eruption of Hakone volcano. *Earth Planets Space* 70 (1), 181.
- Lanari, R., Lundgren, P., Sansosti, E., 1998. Dynamic deformation of Etna volcano observed by satellite radar interferometry. *Geophys. Res. Lett.* 25 (10), 1541–1544.
- Leonov, V., 1995. Lineaments, tectonic fractures, and mechanical behaviour of Kluchevskoi volcano. *Volcanol. Seismol.* 16, 627–648.
- lipman, P.W., Mullineaux, D.R., 1981. The 1980 Eruptions of Mount St. Helens. US Dept. of the Interior, US Geological Survey, Washington.
- lodato, L., Spampinato, L., Harris, A., Calvari, S., Dehn, J., Patrick, M., 2007. The morphology and evolution of the Stromboli 2002–2003 lava flow field: an example of a basaltic flow field emplaced on a steep slope. *Bull. Volcanol.* 69 (6), 661–679.
- lu, Z., Dzurisin, D., 2010. Ground surface deformation patterns, magma supply, and magma storage at Okmok volcano, Alaska, from InSAR analysis: 2. Coercitive deflation, July–August 2008. *J. Geophys. Res.: Solid Earth* 115 (B5).
- Lundgren, P., Rosen, P.A., 2003. Source model for the 2001 flank eruption of Mt. Etna volcano. *Geophys. Res. Lett.* 30 (7).
- Lundgren, P., Berardino, P., Coltellini, M., Fornaro, G., Lanari, R., Puglisi, G., Sansosti, E., Tesauro, M., 2003. Coupled magma chamber inflation and sector collapse slip observed with synthetic aperture radar interferometry on Mt. Etna volcano. *J. Geophys. Res.: Solid Earth* 108 (B5) 1978–2012.
- Lundgren, P., Casu, F., Manzo, M., Pepe, A., Berardino, P., Sansosti, E., Lanari, R., 2004. Gravity and magma induced spreading of Mount Etna volcano revealed by satellite radar interferometry. *Geophys. Res. Lett.* 31 (4).
- Macfarlane, D., Wadge, G., Robertson, D., James, M., Pinkerton, H., 2006. Use of a portable topographic mapping millimetre wave radar at an active lava flow. *Geophys. Res. Lett.* 33 (3).
- MacLeod, N., 1989. Sector-failure eruptions in Indonesian volcanoes. *Geol. Indonesia* 12 (1), 563–601.
- Major, J.J., Pierson, T., Dinehart, R., Costa, J., 2000. Sediment yield following severe volcanic disturbance—a two-decade perspective from Mount St. Helens. *Geology* 28 (9), 819–822.
- Maramai, A., Graziani, L., Tinti, S., 2005. Tsunamis in the Aeolian Islands (southern Italy): a review. *Mar. Geol.* 215 (1–2), 11–21.
- Marsella, M., Baldi, P., Coltellini, M., Fabris, M., 2012. The morphological evolution of the Sciarra del Fuoco since 1868: reconstructing the effusive activity at Stromboli volcano. *Bull. Volcanol.* 74 (1), 231–248.
- Marti, J., Hurliman, M., Ablay, G.J., Gudmundsson, A., 1997. Vertical and lateral collapses on Tenerife (Canary Islands) and other volcanic ocean islands. *Geology* 25 (10), 879–882.
- Massonet, D., Feigl, K.L., 1998. Radar interferometry and its application to changes in the Earth's surface. *Rev. Geophys.* 36, 441–500.
- Masterlark, T., Lu, Z., Rykhus, R., 2006. Thickness distribution of a cooling pyroclastic flow deposit on Augustine Volcano, Alaska: optimization using InSAR, FEMs, and an adaptive mesh algorithm. *J. Volcanol. Geotherm. Res.* 150 (1), 186–201.
- Matías Gómez, R.O., Rose, W.I., Palma, J.L., Escobar-Wolf, R., 2012. Notes on a Map of the 1961–2010 Eruptions of Volcán de Pacaya, Guatemala. The Geological Society of America Digital Map and Chart Series, 10.
- McAlpin, D.B., Meyer, F.J., Gong, W., Beget, J.E., Webley, P.W., 2016. Pyroclastic flow deposits and InSAR: analysis of long-term subsidence at Augustine volcano, Alaska. *Remote Sens.* 9 (1), 4.
- McGuire, W., 1996. Volcano instability: a review of contemporary themes. *Geol. Soc. Lond. Spec. Publ.* 110 (1), 1–23.
- Melekestsev, I., Braitseva, O., 1984. Gigantic rockslide avalanches on volcanoes. *Volcanol. Seismol.* 6, 495–508.
- Merle, O., Borgia, A., 1996. Scaled experiments of volcanic spreading. *J. Geophys. Res.: Solid Earth* 101 (B6), 13805–13817.
- Michel, R., Avouac, J.P., Taboury, J., 1999. Measuring ground displacements from SAR amplitude images: application to the Landers earthquake. *Geophys. Res. Lett.* 26 (7), 875–878.
- Miklius, A., Lisowski, M., Delaney, P.T., Denlinger, R.P., Dvorak, J.J., Okamura, A.T., Sakol, M.K., 1995. Recent inflation and flank movement of Mauna Loa volcano. *Mauna Loa Revealed: Struct. Compos. Hist. Hazards* 199–205.
- Moore, J.G., Normark, W.R., Holcomb, R.T., 1994. Giant hawaiian landslides. *Annu. Rev. Earth Planet. Sci.* 22 (1), 119–144.
- Muller, C., del Potro, R., Biggs, J., Gottsmann, J., Ebmeier, S.K., Guillaume, S., Cattin, P.-H., Van der Laat, R., 2014. Integrated velocity field from ground and satellite geodetic techniques: application to Arenal volcano. *Geophys. J. Int.* 200 (2), 863–879.
- Murray, J.B., Wooller, L.K., 2002. Persistent summit subsidence at Volcán de Colima, México, 1982–1999: strong evidence against Mogi deflation. *J. Volcanol. Geotherm. Res.* 117 (1–2), 69–78.
- Murray, J.B., de Vries, B.V.W., Pitty, A., Sargent, P., Wooller, L., 2018. Gravitational sliding of the Mt. Etna massif along a sloping basement. *Bull. Volcanol.* 80 (4), 40.
- Nave, R., Isaia, R., Vilardo, G., Barclay, J., 2010. Re-assessing volcanic hazard maps for improving volcanic risk communication: application to Stromboli Island, Italy. *J. Maps* 6 (1), 260–269.
- Neall, V.E., 1979. Geological Map of New Zealand: Sheets P19, P20, & P21: New Plymouth, Egmont, and Manaia. Department of Scientific and Industrial Research.
- Neri, M., Lanzafame, G., Acocella, V., 2008. Dyke emplacement and related hazard in volcanoes with sector collapse: the 2007 Stromboli (Italy) eruption. *J. Geol. Soc.* 165 (5), 883–886.
- Neri, M., Casu, F., Acocella, V., Solaro, G., Pepe, S., Berardino, P., Sansosti, E., Caltabiano, T., Lundgren, P., Lanari, R., 2009. Deformation and eruptions at Mt. Etna (Italy): a lesson from 15 years of observations. *Geophys. Res. Lett.* 36 (2).
- Nolesini, T., Di Traglia, F., Del Ventisette, C., Moretti, S., Casagli, N., 2013. Deformations and slope instability on Stromboli volcano: integration of GBInSAR data and analog modeling. *Geomorphology* 180, 242–254.
- Obert, H., Taisne, B., Gottsmann, J., 2015. Deposit loading and its effect on co-eruptive volcano deformation. *Earth Planet. Sci. Lett.* 413, 186–196.
- O'Shea, B., 1954. Ruapehu and the Tangiwai disaster. *N. Z. J. Sci. Technol.* B 36, 174–189.
- Owen, S.E., Bürgmann, R., 2006. An increment of volcano collapse: Kinematics of the 1975 Kalapana, Hawaii, earthquake. *J. Volcanol. Geotherm. Res.* 150 (1–3), 163–185.
- Owen, S., Segall, P., Freymueller, J., Mikijus, A., Denlinger, R., Árnadóttir, T., Sako, M., Bürgmann, R., 1995. Rapid deformation of the south flank of Kilauea volcano, Hawaii. *Science* 267 (5202), 1328–1332.
- Owen, S., Segall, P., Lisowski, M., Miklius, A., Denlinger, R., Sako, M., 2000. Rapid deformation of Kilauea Volcano: global positioning system measurements between 1990 and 1996. *J. Geophys. Res. Solid Earth* 105 (B8), 18983–18998.
- Palmer, B.A., Alloway, B.V., Neall, V.E., 1991. Volcanic Debris Avalanche Deposits in New Zealand—Lithofacies Organization in Unconfined (Wet-Avalanche Flows).
- Paris, R., Ramalho, R.S., Madeira, J., Ávila, S., May, S.M., Rixhon, G., Engel, M., Brückner, H., Herzog, M., Schukraft, G., 2018. Mega-tsunami conglomerates and flank collapses of ocean island volcanoes. *Mar. Geol.* 395, 168–187.
- Peltier, A., Bianchi, M., Kaminski, E., Komorowski, J.C., Rucci, A., Staudacher, T., 2010. PSInSAR as a new tool to monitor pre-eruptive volcano ground deformation: validation using GPS measurements on Piton de la Fournaise. *Geophys. Res. Lett.* 37 (12).
- Peltier, A., Got, J.L., Villeneuve, N., Boissier, P., Staudacher, T., Ferrazzini, V., Walpersdorf, A., 2015. Long-term mass transfer at Piton de la Fournaise volcano evidenced by strain distribution derived from GNSS network. *J. Geophys. Res. Solid Earth* 120 (3), 1874–1889.
- Petley, D., Mantovani, F., Bulmer, M., Zannoni, A., 2005. The use of surface monitoring data for the interpretation of landslide movement patterns. *Geomorphology* 66 (1–4), 133–147.
- Pinel, V., Poland, M.P., Hooper, A., 2014. Volcanology: lessons learned from synthetic aperture radar imagery. *J. Volcanol. Geotherm. Res.* 289, 81–113.
- Poland, M.P., 2015. Magma supply, storage, and transport at shield-stage. Characteristics Hawaiian Volcanoes 179.
- Poland, M.P., Miklius, A., Sutton, A.J., Thornber, C.R., 2012. A mantle-driven surge in magma supply to Kilauea Volcano during 2003–2007. *Nat. Geosci.* 5 (4), 295.
- Poland, M.P., Peltier, A., Bonforte, A., Puglisi, G., 2017. The spectrum of persistent volcanic flank instability: a review and proposed framework based on Kilauea, Piton de la Fournaise, and Etna. *J. Volcanol. Geotherm. Res.* 339, 63–80.
- Ponomareva, V.V., Pevzner, M.M., Melekestsev, I.V., 1998. Large debris avalanches and associated eruptions in the Holocene eruptive history of Shiveluch volcano, Kamchatka, Russia. *Bull. Volcanol.* 59 (7), 490–505.
- Pritchard, M.E., Simons, M., 2004. An InSAR-based survey of volcanic deformation in the southern Andes. *Geophys. Res. Lett.* 31 (15).
- Pritchard, M., Biggs, J., Wauthier, C., Sansosti, E., Arnold, D., Delgado, F., Ebmeier, S., Henderson, S., Stephens, K., Cooper, C., 2018. Towards coordinated regional multi-satellite InSAR volcano observations: results from the Latin America pilot project. *J. Appl. Volcanol.* 7 (1), 5.
- Procter, J., Cronin, S., Zernack, A., Lube, G., Stewart, R., Nemeth, K., Keys, H., 2014. Debris flow evolution and the activation of an explosive hydrothermal system: Te Maari, Tongariro, New Zealand. *J. Volcanol. Geotherm. Res.* 286, 303–316.
- Ramalho, R.S., Quartau, R., Trenhaile, A.S., Mitchell, N.C., Woodroffe, C.D., Avila, S.P., 2013. Coastal evolution on volcanic oceanic islands: a complex interplay between volcanism, erosion, sedimentation, sea-level change and biogenetic production. *Earth Sci. Rev.* 127, 140–170.
- Ramalho, R.S., Winckler, G., Madeira, J., Helffrich, G.R., Hipólito, A., Quartau, R., Adena, K., Schaefer, J.M., 2015. Hazard potential of volcanic flank collapses raised by new megatsunami evidence. *Sci. Adv.* 1 (9), e1500456.
- Rasà, R., 1991. Geomorphological and morpho-structural investigations on the Fossa cone (Vulcano, Aeolian Islands): a first outline. *Acta Vulcanol.* 1, 127–133.
- Raspini, F., Bianchini, S., Ciampalini, A., Del Soldato, M., Solari, L., Novali, F., Del Conte, S., Rucci, A., Ferretti, A., Casagli, N., 2018. Continuous, semi-automatic monitoring of ground deformation using Sentinel-1 satellites. *Sci. Rep.* 8.
- Reid, M.E., 2004. Massive collapse of volcano edifices triggered by hydrothermal pressurization. *Geology* 32 (5), 373–376.
- Reid, M.E., Christian, S.B., Brien, D.L., 2000. Gravitational stability of three-dimensional stratovolcano edifices. *J. Geophys. Res. Solid Earth* 105 (B3), 6043–6056.

- Reid, M.E., Sisson, T.W., Briëن, D.L., 2001. Volcano collapse promoted by hydrothermal alteration and edifice shape, Mount Rainier, Washington. *Geology* 29 (9), 779–782.
- Reid, M.E., Keith, T.E., Kayen, R.E., Iverson, N.R., Iverson, R.M., Briëن, D.L., 2010. Volcano collapse promoted by progressive strength reduction: new data from Mount St. Helens. *Bull. Volcanol.* 72 (6), 761–766.
- Reid, M.E., Christian, S.B., Briëن, D.L., Henderson, S., 2015. Scoops3D—Software to Analyze Three-Dimensional Slope Stability Throughout a Digital Landscape. US Geological Survey, Virginia.
- Risica, G., Speranza, F., Giordano, G., De Astis, G., Lucchi, F., 2018. Palaeomagnetic dating of the Neostromboli succession. *J. Volcanol. Geotherm. Res.* 371, 229–244.
- Rizzo, A.L., Federico, C., Ingugliatti, S., Sollami, A., Tantillo, M., Vita, F., Bellomo, S., Longo, M., Grassa, F., Liuzzo, M., 2015. The 2014 effusive eruption at Stromboli volcano (Italy): inferences from soil CO<sub>2</sub> flux and 3He/4He ratio in thermal waters. *Geophys. Res. Lett.* 42 (7), 2235–2243.
- Robert, G., Ward, B., de Vries, B.V.W., Freile, P., Perotti, L., Clague, J.J., Giardino, M., 2018. Precursory slope distress prior to the 2010 Mount Meager landslide, British Columbia. *Landslides* 15 (4), 637–647.
- Romagnoli, C., Kokelaar, P., Casalbore, D., Chiocci, F.L., 2009. Lateral collapses and active sedimentary processes on the northwestern flank of Stromboli volcano, Italy. *Mar. Geol.* 265 (3–4), 101–119.
- Roobol, M., Wright, J., Smith, A., 1983. Calderas or gravity-slide structures in the Lesser Antilles island arc? *J. Volcanol. Geotherm. Res.* 19 (1–2), 121–134.
- Rotonda, T., Tommasi, P., Boldini, D., 2009. Geomechanical characterization of the volcaniclastic material involved in the 2002 landslides at Stromboli. *J. Geotech. Geoenvir.* 136 (2), 389–401.
- Sato, H., Fujii, T., Nakada, S., 1992. Crumbling of dacite dome lava and generation of pyroclastic flows at Unzen volcano. *Nature* 360 (6405), 664.
- Schaefer, L.N., Oomen, T., Corazzato, C., Tibaldi, A., Escobar-Wolf, R., Rose, W.I., 2013. An integrated field-numerical approach to assess slope stability hazards at volcanoes: the example of Pacaya, Guatemala. *Bull. Volcanol.* 75 (6), 1–18.
- Schaefer, L., Lu, Z., Oomen, T., 2015a. Dramatic volcanic instability revealed by InSAR. *Geology* 43 (8), 743–746.
- Schaefer, L.N., Kendrick, J.E., Lavallée, Y., Oommen, T., Chigna, G., 2015b. Geomechanical rock properties of a basaltic volcano. *Name: Front. Earth Sci.* 3, 29.
- Schaefer, L., Lu, Z., Oommen, T., 2016. Post-eruption deformation processes measured using ALOS-1 and UAVSAR InSAR at Pacaya volcano, Guatemala. *Remote Sens.* 7 (11) (In press).
- Schaefer, L., Wang, T., Escobar-Wolf, R., Oommen, T., Lu, Z., Kim, J., Lundgren, P., Waite, G., 2017. Three-dimensional displacements of a large volcano flank movement during the May 2010 eruptions at Pacaya Volcano, Guatemala. *Geophys. Res. Lett.* 44 (1), 135–142.
- Schuster, R.L., Salcedo, D.A., Valenzuela, L., 2002. Overview of catastrophic landslides of South America in the twentieth century. *Catastrophic Landslides: Effects Occurrence Mech.* 15, 1–33.
- Sekiya, S. and Kikuchi, Y. (1889) The eruption of Bandai-san. na.
- Shea, T., Van Wyk De Vries, B., 2010. Collapsing volcanoes: the sleeping giants' threat. *Geol. Today* 26 (2), 72–77.
- Shirzaei, M., Walter, T., Nankali, H., Holohan, E., 2011. Gravity-driven deformation of Damavand volcano, Iran, detected through InSAR time series. *Geology* 39 (3), 251–254.
- Siebert, L., 1984. Large volcanic debris avalanches and associated eruptive phenomena. In: *Monitoring and Mitigation of Volcano Hazard*. Springer, Berlin, pp. 541–572.
- Siebert, L., 1996. Hazards of large volcanic debris avalanches and associated eruptive phenomena. In: *Monitoring and Mitigation of Volcano Hazards*. Springer, pp. 541–572.
- Siebert, L., Glicken, H., Ui, T., 1987. Volcanic hazards from Bezymianny-and Bandai-type eruptions. *Bull. Volcanol.* 49 (1), 435–459.
- Siebert, L., Alvarado, G.E., Vallance, J.W., de Vries, B.V.W., 2006. Large-volume volcanic edifice failures in Central America and associated hazards. *Volcanic Hazards Central Am.* 412, 1.
- Silver, E., Day, S., Ward, S., Hoffmann, G., Llanes, P., Driscoll, N., Applegate, B., Saunders, S., 2009. Volcano collapse and tsunami generation in the Bismarck volcanic arc, Papua New Guinea. *J. Volcanol. Geotherm. Res.* 186 (3–4), 210–222.
- Solari, L., Del Soldato, M., Bianchini, S., Ciampalini, A., Ezquerro, P., Montalti, R., Raspini, F., Moretti, S., 2018. From ERS 1/2 to Sentinel-1: subsidence monitoring in Italy in the last two decades. *Front. Earth Sci.* 6, 149.
- Solaro, G., Acocella, V., Pepe, S., Ruch, J., Neri, M., Sansosti, E., 2010. Anatomy of an unstable volcano from InSAR: multiple processes affecting flank instability at Mt. Etna, 1994–2008. *J. Geophys. Res.: Solid Earth* 115 (B10) 1978–2012.
- Sosio, R., Crosta, G.B., Hungr, O., 2012. Numerical modeling of debris avalanche propagation from collapse of volcanic edifices. *Landslides* 9 (3), 315–334.
- Sparks, R., Barclay, J., Calder, E., Herd, R., Komorowski, J., Luckett, R., Norton, G., Ritchie, L., Voight, B., Woods, A., 2002. Generation of a debris avalanche and violent pyroclastic density current on 26 December (Boxing Day) 1997 at Soufrière Hills Volcano, Montserrat. *Geol. Soc. Lond. Mem.* 21 (1), 409–434.
- Stevens, N., Wadge, G., Williams, C., 2001. Post-emplacement lava subsidence and the accuracy of ERS InSAR digital elevation models of volcanoes. *Int. J. Remote Sens.* 22 (5), 819–828.
- Swanson, D.A., Duffield, W.A., Fiske, R.S., 1976. Displacement of the South Flank of Kilaua Volcano; the Result of Forceful Intrusion of Magma into The Rift Zones (No. 963). US Govt. Print. Off.
- Taddeucci, J., Palladino, D., Sottili, G., Bernini, D., Andronico, D., Cristaldi, A., 2013. Linked frequency and intensity of persistent volcanic activity at Stromboli (Italy). *Geophys. Res. Lett.* 40 (13), 3384–3388.
- Tarchi, D., Casagli, N., Fortuny-Guasch, J., Guerri, L., Antonello, G., Leva, D., 2008. Ground deformation from ground-based SAR interferometry. The Stromboli Volcano: an integrated study of the 2002–2003 eruption. *182*, 359–372.
- Ter-Stepanian, G., 1966. Types of Depth Creep of Slopes in Rock Masses, 1st ISRM Congress. International Society for Rock Mechanics.
- Tibaldi, A., 2001. Multiple sector collapses at Stromboli volcano, Italy: how they work. *Bull. Volcanol.* 63 (2–3), 112–125.
- Tibaldi, A., Bistacchi, A., Pasquare, F.A., Vezzoli, L., 2006. Extensional tectonics and volcano lateral collapses: insights from Ollagüe volcano (Chile-Bolivia) and analogue modelling. *Terra Nova* 18 (4), 282–289.
- Tibaldi, A., Corazzato, C., Marani, M., Gamberi, F., 2009. Subaerial-submarine evidence of structures feeding magma to Stromboli Volcano, Italy, and relations with edifice flank failure and creep. *Tectonophysics* 469 (1–4), 112–136.
- Tinti, S., Maramai, A., Armigliato, A., Graziani, L., Manucci, A., Pagnoni, G., Zaniboni, F., 2006a. Observations of physical effects from tsunamis of December 30, 2002 at Stromboli volcano, southern Italy. *Bull. Volcanol.* 68 (5), 450–461.
- Tinti, S., Pagnoni, G., Zaniboni, F., 2006b. The landslides and tsunamis of the 30th of December 2002 in Stromboli analysed through numerical simulations. *Bull. Volcanol.* 68 (5), 462–479.
- Tofani, V., Raspini, F., Catani, F., Casagli, N., 2013. Persistent Scatterer Interferometry (PSI) technique for landslide characterization and monitoring. *Remote Sens.* 5 (3), 1045–1065.
- Tommasi, P., Baldi, P., Chiocci, F.L., Coltellini, M., Marsella, M., Pompilio, M., Romagnoli, C., 2005. The landslide sequence induced by the 2002 eruption at Stromboli volcano. In: *Landslides*. Springer, pp. 251–258.
- Ui, T., 1983. Volcanic dry avalanche deposits—identification and comparison with non-volcanic debris stream deposits. *J. Volcanol. Geotherm. Res.* 18 (1–4), 135–150.
- Ui, T., Yamamoto, H., Suzuki-Kamata, K., 1986. Characterization of debris avalanche deposits in Japan. *J. Volcanol. Geotherm. Res.* 29 (1–4), 231–243.
- Vallance, J.W., Siebert, L., Rose, W.I., Girón, J.R., Banks, N.G., 1995. Edifice collapse and related hazards in Guatemala. *J. Volcanol. Geotherm. Res.* 66 (1), 337–355.
- Vezzoli, L., Corazzato, C., 2016. Geological constraints of a structural model of sector collapse at Stromboli volcano, Italy. *Tectonics* 35 (9), 2070–2081.
- Voight, B., 2000. Structural stability of andesite volcanoes and lava domes. *philosophical transactions: mathematical. Phys. Eng. Sci.* 358 (1770), 1663–1703.
- Voight, B., Elsworth, D., 1997. Failure of volcano slopes. *Geotechnique* 47 (1), 1–31.
- Voight, B., Janda, R., Douglass, P., 1983. Nature and mechanics of the Mount St Helens rockslope-avalanche of 18 May 1980. *Geotechnique* 33 (3), 243–273.
- Voight, B., Komorowski, J., Norton, G., Belousov, A., Belousova, M., Boudon, G., Francis, P., Franz, W., Heinrich, P., Sparks, R., 2002. The 26 December (Boxing Day) 1997 sector collapse and debris avalanche at Soufrière Hills volcano, Montserrat. *Geol. Soc. Lond. Mem.* 21 (1), 363–407.
- Wadge, G., Webley, P., James, I., Bingley, R., Dodson, A., Waugh, S., Veneboer, T., Puglisi, G., Mattia, M., Baker, D., 2002. Atmospheric models, GPS and InSAR measurements of the tropospheric water vapour field over Mount Etna. *Geophys. Res. Lett.* 29 (19).
- Wadge, G., Macfarlane, D., Robertson, D., Hale, A., Pinkerton, H., Burrell, R., Norton, G., James, M., 2005. AVTIS: a novel millimetre-wave ground based instrument for volcano remote sensing. *J. Volcanol. Geotherm. Res.* 146 (4), 307–318.
- Wadge, G., Macfarlane, D., Odber, H., James, M., Hole, J., Ryan, G., Bass, V., De Angelis, S., Pinkerton, H., Robertson, D., 2008. Lava dome growth and mass wasting measured by a time series of ground-based radar and seismicity observations. *J. Geophys. Res. Solid Earth* 113 (B8).
- Ward, S.N., Day, S., 2003. Ritter Island volcano—lateral collapse and the tsunami of 1888. *Geophys. J. Int.* 154 (3), 891–902.
- Wardman, J., Sword-Daniels, V., Stewart, C., Wilson, T., 2012. Impact Assessment of the May 2010 Eruption of Pacaya Volcano. University of Canterbury. Geological Sciences, Guatemala.
- Welch, M.D., Schmidt, D.A., 2017. Separating volcanic deformation and atmospheric signals at Mount St. Helens using Persistent Scatterer InSAR. *J. Volcanol. Geotherm. Res.* 344, 52–64.
- Williams, S., Bock, Y., Fang, P., 1998. Integrated satellite interferometry: tropospheric noise, GPS estimates and implications for interferometric synthetic aperture radar products. *J. Geophys. Res. Solid Earth* 103 (B11), 27051–27067.
- Witham, C.S., 2005. Volcanic disasters and incidents: a new database. *J. Volcanol. Geotherm. Res.* 148 (3–4), 191–233.
- Wnuk, K., Wauthier, C., 2017. Surface deformation induced by magmatic processes at Pacaya Volcano, Guatemala revealed by InSAR. *J. Volcanol. Geotherm. Res.* 344, 197–211.
- Wunderman, R.L., Rose, W.I., 1984. Amatitlán, an actively resurgent cauldron 10 km south of Guatemala City. *J. Geophys. Res. Solid Earth* 89 (B10), 8525–8539.
- Zakšek, K., Hort, M., Lorenz, E., 2015. Satellite and ground based thermal observation of the 2014 effusive eruption at Stromboli volcano. *Remote Sens.* 7 (12), 17190–17211.
- Zernack, A., Cronin, S., Neall, V., Procter, J., 2011. A medial to distal volcaniclastic record of an andesite stratovolcano: detailed stratigraphy of the ring-plain succession of south-West Taranaki, New Zealand. *Int. J. Earth Sci.* 100 (8), 1937–1966.
- Zhao, C., Lu, Z., Zhang, Q., de La Fuente, J., 2012. Large-area landslide detection and monitoring with ALOS/PALSAR imagery data over Northern California and Southern Oregon, USA. *Remote Sens. Environ.* 124, 348–359.
- Zinno, I., Bonano, M., Buonanno, S., Casu, F., De Luca, C., Manunta, M., Manzo, M., Lanari, R., 2018. National Scale Surface Deformation Time Series Generation through Advanced DinSAR Processing of Sentinel-1 Data within a Cloud Computing Environment. *IEEE Transactions on Big Data*.